1995A&A...302..223J

Astron. Astrophys. 302, 223–242 (1995)

ASTRONOMY
AND
ASTROPHYSICS

Physical and chemical structure of the IC 63 nebula

II. Chemical models

David J. Jansen[1], **Ewine F. van Dishoeck**[1], **John H. Black**[2], **Marco Spaans**[1], **and Craig Sosin**[3] *

[1] Leiden Observatory, P.O. Box 9513, NL- 2300 RA Leiden, The Netherlands
[2] Steward Observatory, University of Arizona, Tucson, AZ 85721, USA
[3] Division of Geology and Planetary Sciences, California Institute of Technology, Pasadena CA 91125, USA

Received 10 January 1995 / Accepted 25 February 1995

Abstract. Chemical models are presented for the photon dominated region (PDR) IC 63, a small isolated molecular cloud located close to the B0.5 IVpe star γ Cas for which we have presented observations of various molecular species in an earlier paper, and for which observations of ionized and neutral atomic carbon, as well as additional CO observations, are available. The models treat the photoexcitation and photodissociation processes in detail, and use the actual γ Cas radiation field as measured by the S2-68 and IUE satellites. The heating and cooling balance of the cloud is taken explicitly into account. The computed H_2 ultraviolet fluorescent spectrum agrees well with observations, thus providing support for the inferred physical structure. Effects of the radiation field, elemental depletions, density and cosmic ray ionization rate on the chemistry are discussed. Several distinct chemical zones are found with depth into the cloud. At the edge, most species are in ionized atomic form, and reactions with C^+ drive the chemistry. Deeper into the cloud around $A_V \approx 2$ mag, carbon is transformed into neutral atomic carbon and CO. At this same depth, the abundances of radicals such as CH, CH_2, CH_3, CN and C_2H peak. They rapidly decline at larger depths due to reactions with atomic oxygen. Only species such as CH_4, H_2CO, and HCN, which do not react with O, have large abundances deep into the cloud. As a result, the CN/HCN abundance ratio varies strongly with depth. Most observed column densities can be reproduced to within a factor of a few, and in many cases even better than a factor of two. Only the chemistry of sulfur-bearing molecules does not fit the observations: if the sulfur depletion is fixed to reproduce the observed CS column density, the model H_2S column density is too low and that of SO too high by an order of magnitude. The resulting temperature structure in the one-dimensional plane-parallel models agrees reasonably well with that inferred from observations. Improved comparison is obtained in two-dimensional models which take the actual geometry of the region into account. The results of such geometrical models are presented, and are compared with those obtained in the one-dimensional case. In general, the agreement between one-dimensional and two-dimensional models is good enough to justify the one-dimensional approximation in a simple cloud like IC 63, whereas for more complex clouds the actual geometry might become very important.

Key words: ISM: clouds – ISM: IC 63 – ISM: molecules – molecular processes – reflection nebulae

1. Introduction

The physical and chemical structure of photon dominated regions (PDRs) is primarily controlled by ultraviolet photons, as implied by their name. These photons are responsible for heating the cloud and they drive the chemistry through photodissociation and photoionization reactions, which create radicals and ions. Although many theoretical (e.g., Tielens & Hollenbach 1985; van Dishoeck & Black 1988; Sternberg & Dalgarno 1989; Le Bourlot et al. 1993) and observational (e.g., Keene et al. 1985; Stutzki et al. 1988; Genzel et al. 1991; Tauber et al. 1994; Köster et al. 1994) studies have been made of their physical structure and the $C^+ \rightarrow C \rightarrow CO$ transition, comparatively little work has been done on the behavior of other molecular abundances with depth into PDRs. Sternberg & Dalgarno (1995) have investigated theoretical models for a dense cloud — $n = 1 \times 10^6\ \mathrm{cm}^{-3}$ — that is irradiated by a very strong ultraviolet radiation field — $I = 2 \times 10^5 I(\mathrm{Draine})$. The only PDR which has been studied in some chemical detail both observationally and theoretically is NGC 7023 (Fuente et al. 1993). We present here a study of a small, isolated reflection nebula, IC 63, which may serve as a prototype for studying PDR chemistry.

IC 63 is a reflection nebula associated with the B0.5 IVpe star γ Cas (HD 5394), which lies at a distance of approximately 230 pc. The projected distance between IC 63 and the star is $\sim 20'$, corresponding to 1.3 pc. Due to the proximity of the star, the cloud is exposed to approximately 650 times the mean galactic

---

* Present address: Dept. of Astronomy, University of California, Berkeley, CA 94720, USA

ultraviolet radiation field. The molecular lines are narrow (≈ 1 km s^{-1}), indicating the absence of shocks that might otherwise have influenced the chemistry. The cloud is therefore easier to study and less confused than well known PDRs like M 17, which is very distant and has embedded sources which may influence the chemistry, or NGC 2023, which is viewed mostly face-on.

In a previous paper (Jansen et al. 1994, hereafter Paper I) we presented millimeter and submillimeter observations of various molecules towards the PDR IC 63. We have used these observations to determine molecular column densities for this source, as well as to put constraints on the temperature and density. All observations can be fit with a single column averaged density and temperature, $n(H_2) \approx (5 \pm 2) \times 10^4$ cm^{-3} and $T \approx (50 \pm 20)$ K. The derived molecular hydrogen column density is $N(H_2) = (5 \pm 2) \times 10^{21}$ cm^{-2} or $A_V \approx (6.7 \pm 2.3)$ mag. Observations of lines of neutral and ionized carbon as well as high-J CO lines will be presented in a separate paper (Jansen et al. 1995, Paper III). Combined with the low-J CO observations of Paper I, they fully constrain the amount of gas-phase carbon in this source, an important ingredient in the chemistry.

Our chemical models are based on the diffuse and translucent cloud models of van Dishoeck & Black (1986, 1988, 1989), but extended to higher densities and stronger ultraviolet radiation fields. They differ from earlier PDR models (e.g., Tielens & Hollenbach 1985; Fuente et al. 1993) in that we perform a full calculation of the photodissociation rates for each depth step, using the actual radiation field provided by γ Cas as a function of wavelength rather than just a fitted exponential with an enhancement with respect to a standard galactic radiation field. The depth dependence of the rates is computed by considering shielding by dust as well as self-shielding and mutual shielding of H_2, CO and its isotopes. The heating and cooling processes are considered explicitly, in contrast with the earlier work of van Dishoeck & Black (1986), and include heating due to small grains or large molecules such as polycyclic aromatic hydrocarbons (PAHs) (d'Hendecourt & Leger 1987; Bakes & Tielens 1994). Compared with the detailed chemical models of Sternberg & Dalgarno (1995), the current models refer to a cloud with a factor of 10 lower density and exposed to a factor of 100 less radiation.

Another new feature of our models is the extension to two dimensions. Since IC 63 is a small cloud, radiation from γ Cas and from the general interstellar radiation field can enter from all sides. An independent code has been written by Spaans (1995), which treats the radiative transfer in both lines and continuum by a Monte Carlo method for an arbitrary geometry. Although the chemical network used in this model is less extensive than that in the one-dimensional models, it can be used to investigate the geometrical effects on both the chemical and the thermal structure of the cloud.

In Sect. 2, the main observational results of paper I are reiterated and additional data that have become available are discussed. In Sect. 3, the observational data on the radiation field incident on IC 63 are presented, whereas in Sect. 4, the details of the modeling procedure are outlined. In Sect. 5, the results of one-dimensional plane-parallel, time-independent models are presented and compared with observations, whereas in Sect. 6, the two-dimensional calculations are discussed. Finally, the conclusions of this work are summarized in Sect. 7.

2. Summary of observations

The column densities of the various molecules derived in Paper I at the $(0'', 0'')$ position are summarized in Table 1. The beam sizes for these observations were typically 20″–30″. In addition, the column densities of C and C^+, for which observations will be reported in paper III, are included. Another important species in the chemistry is atomic hydrogen, which McCutcheon et al. (1994, priv. comm.) have recently measured at 21 cm at the Dominion Radio Astrophysical Observatory (DRAO) radio synthesis telescope. These observations show that the column density of atomic hydrogen in the direction of IC 63, as measured in a $1'$ beam, is 6.9×10^{20} cm^{-2}, assuming the line is optically thin. This is, however, an upper limit to the atomic hydrogen column density of IC 63 itself, due to beam dilution and confusion in the plane of our galaxy. Neighboring regions on the sky show atomic hydrogen column densities of $(3 \pm 1) \times 10^{20}$ cm^{-2}. Therefore we estimate that the atomic hydrogen column density of IC 63 itself is approximately $(4 \pm 2) \times 10^{20}$ cm^{-2}.

In Paper I, column densities were derived for both high and low electron abundance, $n(e)/n(H_2) = 1 \times 10^{-4}$ and $= 1 \times 10^{-5}$ respectively. As will be shown in the discussion of the chemistry, the electron fraction is a few$\times 10^{-5}$ at the edge closest to the star, decreasing to 1×10^{-7} at the other side. Therefore, we use the low electron fraction column densities from Paper I. The uncertainty in the derived column densities is at least 30 % due to the calibration of the observations, but may range up to a factor of 2 for molecules like HCN which are very sensitive to the electron fraction in this temperature and density regime. After Paper I appeared we noted a typographical error in the upper limit listed for SO_2. This value should be 1.5×10^{13} cm^{-2} instead of 1.5×10^{12} and has been corrected in this paper.

3. The ultraviolet spectrum of γ Cas

Since the cross sections for the photo-processes of the individual molecules depend strongly on wavelength, an accurate calculation of the chemistry needs to take into account the actual spectral distribution of the radiation incident on the cloud. The ultraviolet spectrum of a B0.5 star like γ Cas has a very similar shape to the mean galactic radiation field as given by Draine (1978) or Mathis et al. (1983), because early B stars are the most effective contributors to the radiation field (van Dishoeck 1994). If we assume that the projected distance between IC 63 and γ Cas is the true distance, then IC 63, at 1.3 pc from the star, will receive about 650 times the Draine field, or 900 times the Mathis et al. field at a wavelength of 1000 Å. These radiation fields are shown in Fig. 2, in units of photons cm^{-2} s^{-1} Hz^{-1}. The Draine (1978) field is supplemented for $\lambda > 2000$ Å with the unattenuated interstellar radiation field as given by van Dishoeck & Black (1982).

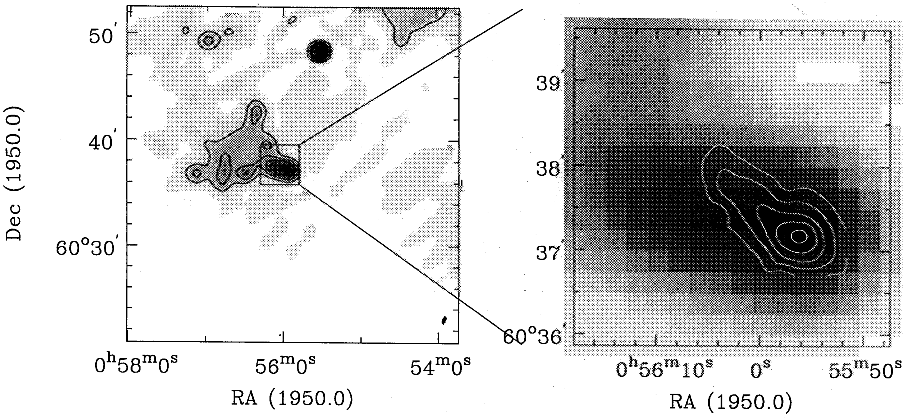

Fig. 1. left: IRAS 60 μm image of IC 63. This image was obtained using the HIRAS technique (Bontekoe et al. 1994). The star γ Cas is located just outside the map, at $\alpha = 0^h53^m40^s$, $\delta = 60°26'48''$. **right**: Overlay of the central part of the IRAS 60 μm map with the ^{12}CO 2 → 1 map (paper I). Observations of other molecules were only obtained at the peak of the CO map, located at $\alpha = 0^h55^m58^s$, $\delta = 60°37'7''$

Table 1. IC 63 column densities (cm^{-2}) at the $(0'', 0'')$ position

Species	Observed
H	$\approx 4.0 \times 10^{20}$
H_2	5.0×10^{21}
C	3.7×10^{16a}
C^+	2.0×10^{17a}
CO	3.0×10^{17a}
^{13}CO	3.9×10^{15}
$C^{18}O$	5.0×10^{14}
CS	9.5×10^{12}
CN	2.7×10^{13}
HCN	4.0×10^{13}
HNC	1.1×10^{13}
HCO^+	8.0×10^{12}
H_2CO	5.0×10^{12}
C_2H	1.8×10^{13}
N_2H^+	2.9×10^{11}
H_2S	7.3×10^{12}
SO	$<5.0 \times 10^{12}$
SO_2	$<1.5 \times 10^{13}$
SiO	$<1.0 \times 10^{12}$
CH_3OH	$<1.9 \times 10^{13}$
CH_3CN	$<7.4 \times 10^{12}$
HC_3N	$<9.3 \times 10^{12}$
HNCO	$<2.8 \times 10^{12}$

[a] to be published (paper III)

The actual spectrum of γ Cas has been measured by Code & Meade (1979) in the range 1200-3580 Å using the Orbiting Astronomical Observatory 2 satellite (OAO-2). Additional observations covering the 1360-2740 Å range were made using the S2-68 satellite, and have been published in the supplement of the UV Bright Star Catalogue (Macau-Hercot et al. 1978). Also, IUE (International Ultraviolet Explorer) observations of γ Cas have been obtained by Waters & Telting (1993). Unfortunately, the star is too bright for IUE's normal low resolution spectral mode, and has therefore been observed in "trailed" mode, where the telescope slewed along the source to keep integration times short enough to avoid saturation of the detectors. This has the side effect that the absolute calibration is lost. In the reduction of these spectra we assumed that the calibration problem causes the spectrum to differ from the true spectrum by a constant factor over the whole wavelength range (1150-3350 Å). We derived this factor from comparison with the S2-68 spectrum for each of the IUE observations separately. The resulting spectrum, shown in Fig. 2, is the combination of 4 SWP spectra (1150-1950 Å) and 5 LWP spectra (1850-3350 Å). As can be seen from Fig. 2, the spectra are in good agreement for $\lambda \gtrsim 2000$ Å, but in the important range of 1150-2000 Å the IUE and S2-68 spectra are significantly lower than the OAO-2 spectrum (Code & Meade 1979).

A critical part of the spectrum for computing the photodissociation rates of CO and H_2 and the photoionization rate of atomic carbon is the 912-1100 Å range. A factor of 2 increase in the intensity of the radiation field here translates almost directly to a factor of 2 lower CO abundance in the region where photodissociation is the dominant removal mechanism for this molecule. A broad-band measurement with a filter covering 912-1075 Å has been made by Troy et al. (1975) in a rocket experiment. The measured value of 6.8×10^{-6} photons cm^{-2} s^{-1} Hz^{-1} is higher than a simple extrapolation from the observed spectra would yield. Troy et al. (1975) state that this value has an equivalent wavelength of 950 Å. Since it is the only available measurement, we use it to extrapolate the OAO-2, S2-68 and IUE radiation fields. The observed spectra have been corrected for interstellar extinction, $E(B-V) = 0.03$ mag, by extrapolation of the extinction curve to small wavelengths.

Note that these spectra do not take the variability of γ Cas into account; the star shows changes in intensity on time scales ranging from hours to years. The short-term variations are probably due to inhomogeneities in the rotating circumstellar envelope; these variations are of order 0.1 % (Piirola 1979). The star has also gone through two phases of Balmer emission outbursts this century, the most recent one started in 1946 and is still continuing (Telting & Kaper 1994). Variability may be important at the edge of the cloud, where chemical timescales are short enough to be able to follow the variations in the radiation field to some extent. Deeper into the cloud, the chemistry is slower, and it will more or less reflect the time averaged radiation field, with the influence of the variability diminished. In the current time-independant models, this effect has not been taken into account.

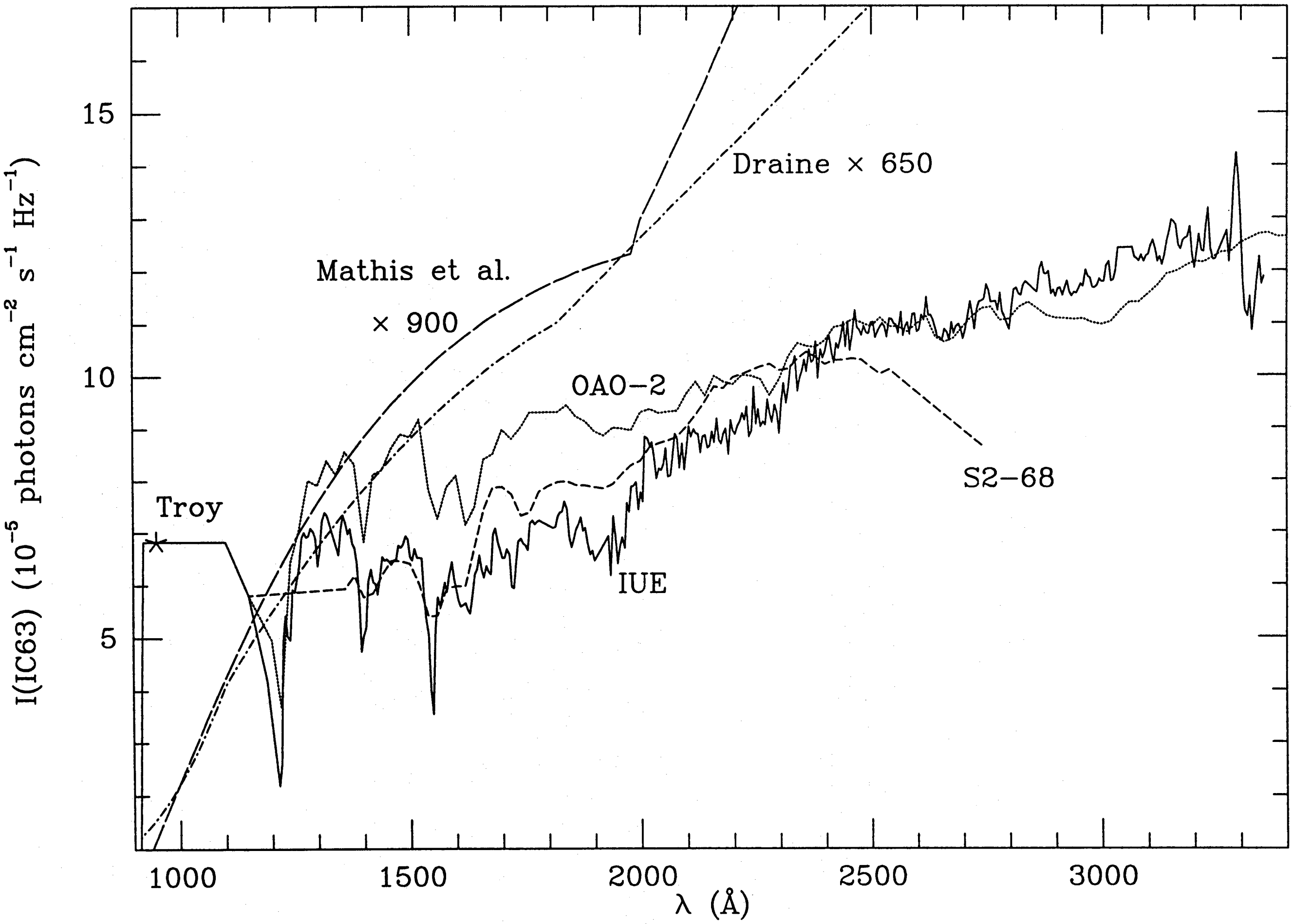

Fig. 2. The radiation field of γ Cas compared with scaled versions of the mean galactic radiation field. The curves shown are: IUE (solid); S2-68 (short dash); OAO-2 (dotted); 650 × Draine (dash-dotted) and 900 × Mathis et al. (long dash)

We have ignored the H-ionizing photons ($\lambda < 912$ Å) from γ Cas because these will be used up in a distinct H II region that is largely outside the PDR. It is known that γ Cas is an X-ray source with a luminosity of $L_X \approx 10^{33}$ erg s^{-1} (White et al. 1982; Murakami et al. 1986; Parmar et al. 1993; Horiguchi et al. 1994). In principle, the stellar X-rays could penetrate deeply into the PDR and affect its ion chemistry. In fact, the observed X-ray spectrum, corrected for interstellar absorption and extrapolated to photon energies as small as $h\nu$ = 0.25 keV, yields an unshielded photoionization rate of H of only 2×10^{-19} s^{-1} at a distance 1.3 pc from the star. This rate is significantly smaller than that due to penetrating Galactic cosmic rays, $\geq 10^{-17}$ s^{-1}; therefore, the X-radiation from γ Cas can be ignored.

4. H_2 fluorescent spectrum

The strong ultraviolet radiation from γ Cas can excite the H_2 molecules in the IC 63 cloud into the $B^1\Sigma_u^+$ and $C^1\Pi_u$ electronic states. The ultraviolet fluorescence back to the $X^1\Sigma_g^+$ ground state following these absorptions has been observed by Witt et al. (1989) using the IUE satellite. Witt et al. modeled the H_2 emission with a low density ($n(H_2) = 0.15$ cm^{-3}) mostly atomic cloud, but Sternberg (1989) and Sosin et al. (1990) pointed out that the density needs to be much higher, $> 10^4$ cm^{-3}, if H_2 self-shielding is properly included. The fluorescence process also leads to strong H_2 infrared vibration-rotation lines, but no detections have yet been reported for IC 63.

The amount of ultraviolet pumping — and thus the intensities of the H_2 ultraviolet and infrared lines — depends mainly on the density and the strength of the incident radiation field (see Black & van Dishoeck 1987 and Sternberg 1988 for the infrared lines, and Sternberg 1989 for the ultraviolet lines). In the regime appropriate for IC 63, the intensity of these lines scales nearly linearly with both parameters. Thus, the H_2 ultraviolet observations can be used as a further test of the physical conditions in IC 63.

We have modeled both the ultraviolet and infrared fluorescent spectra of H_2 following the method described by Black & van Dishoeck (1987). All vibration-rotation lines of H_2 $X^1\Sigma_g^+$ with $J \leq 16$ were taken into account, leading to > 20000 ultraviolet pumping lines in the Lyman and Werner systems. In the subsequent calculation of the ultraviolet fluorescent spectrum, both line and continuum emission processes were included. Improved values for the bound-bound and bound-continuum transition probabilities were computed using the potential energy curves of Wolniewicz & Dressler (1988) including adiabatic corrections, together with the transition dipole moment functions of Dressler & Wolniewicz (1985). The resulting oscillator strengths differ by only a few percent from the values of Allison & Dalgarno (1970). The spectra were computed in the optically thin limit, and were corrected for ultraviolet extinction. Because most of the ultraviolet emission originates close to the surface of the cloud ($A_V < 0.5$ mag), the correction factor is small. A Doppler parameter $b = 2\,\mathrm{km\,s^{-1}}$ was adopted.

In paper I, the density was derived to be $n(H_2) \approx (5 \pm 2) \times 10^4\,\mathrm{cm^{-3}}$. If $n_H = 2n(H_2) = 10^5\,\mathrm{cm^{-3}}$ is used together with the actual γ Cas radiation field (cf. Sect. 3) or with 650 times the Draine (1978) field, the resulting H_2 ultraviolet intensity is too large by about a factor of 3-4 compared with observations. This suggests that a somewhat lower density is appropriate for the region where the H_2 emission originates. In Fig. 3 (top), the H_2 fluorescent spectrum for a model with $n_H = 4 \times 10^4\,\mathrm{cm^{-3}}$ is presented. In order to match the observed peak intensity at 1600 Å, a small additional extinction was assumed between the star and the cloud. The model reproduces the observed spectrum of Witt et al. (1989) remarkably well, given the S/N of the data. In Fig. 3 (bottom), the H_2 fluorescent spectrum obtained with the actual γ Cas radiation field is compared with that resulting from use of 650 times the Draine field. At longer wavelengths around 1600 Å, the differences are small, but at short wavelengths around 1000 Å, the γ Cas field results in higher intensities due to more efficient excitation into the Werner system. Figure 3 (bottom) also shows the contribution of the continuum emission separately. Although it contributes only $\sim$ 10% of the total emission, it significantly affects the spectrum between 1400 and 1700 Å.

The fluorescence model has assumed a constant temperature T = 50 K. The temperature in the H_2-emitting zone may be higher than this value. The rotational population distributions are sensitive to temperature and will be partly preserved in the fluorescence spectrum, most visibly in the infrared lines, which can be resolved. New observational data, together with a more detailed model, might provide a probe of the temperature in the warm part of the PDR. For the best fitting model, the predicted strengths of the H_2 infrared lines are (1,0) S(1)= 6.2×10^{-6} and (2,1) S(1)= $3.3 \times 10^{-6}\,\mathrm{erg\,s^{-1}\,cm^{-2}\,sr^{-1}}$. Intensities of other lines can be obtained by scaling with respect to the (1,0) S(1) line using Table 3 of Black & van Dishoeck (1987).

5. Chemical models

5.1. One-dimensional model

The chemical calculations have been performed using a time-independent chemistry code. Most of the models were calculated in one dimension, essentially treating the cloud as an infinite plane parallel slab of material, with one side facing the star, and thus experiencing an isotropic radiation field. The depth into the cloud is parameterized by the H_2 column density (or, alternatively, A_V, the visual extinction), measured from the edge of the PDR inwards. This edge is defined as the location where all hydrogen is in neutral atomic form, and thus no photons shortward of 912 Å remain in the spectrum.

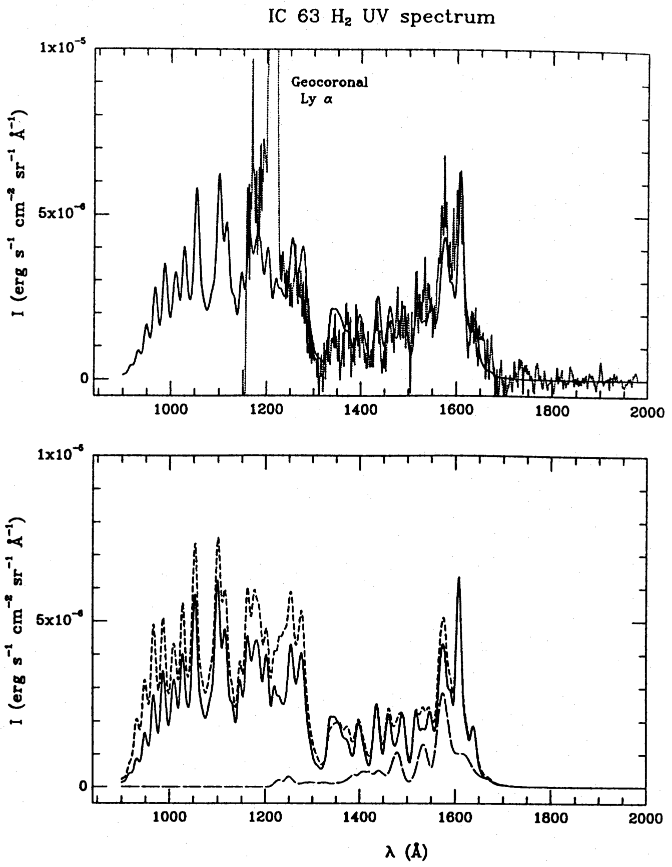

Fig. 3. Top: Comparison of the computed H_2 ultraviolet fluorescent spectrum (full line) with the observed spectrum by Witt et al. (1989) (dotted lines). The model has $n_H = 4 \times 10^4\,\mathrm{cm^{-3}}$, T = 50 K and uses the Draine (1978) radiation field enhanced by a factor of 650. **Bottom:** Comparison of model spectra obtained with the γ Cas radiation field from the IUE satellite (dashed line) and with 650 times the Draine (1978) radiation field (full line). The contribution of the continuum emission to the latter spectrum is shown separately (long dashed line)

The calculations start at the side closest to the star. At every depth step the program calculates the amount of ultraviolet radiation that can penetrate into this layer, using the attenuation of the radiation field by the dust, and computes the corresponding photo-rates, taking into account self-shielding, mutual shielding and shielding by coincident lines of H and H_2. The other rates are read from a reaction database. All these reaction rates together form a matrix R ; the equation to be solved is:

$$X_{n,i+1} = R_n \cdot X_{n,i} \tag{1}$$

where $X_{n,i}$ is the vector of the abundances at depth step n and iteration i. Note that the fractional abundances used in this code are relative to the total density: $X(m) = n(m)/n_H$.

The main parameters entering the models are: the total density $n_H = n(H) + 2n(H_2)$, the total molecular hydrogen column density $N(H_2)$ (or, alternatively, the visual extinction A_V), the incident radiation field and the depletions of the elements. The code calculates the temperature structure of the cloud from the heating and cooling balance (see below), so that the temperature does not enter the calculations as a parameter. As discussed before, $n_{\rm H}$, $N({\rm H}_2)$ and the radiation field are constrained by observations, so only the cosmic ray ionization rate ζ and the elemental depletions (except that of carbon) remain as free parameters.

The adopted reaction network is based on that used by van Dishoeck & Black (1986, 1988) to model the chemistry of translucent clouds, combined with the sulfur chemistry as described by Drdla et al. (1989), which was taken from Prasad & Huntress (1980, 1982). Updated reaction rates from the literature are included (HNC + O: Schilke et al. 1992; neutral-neutral reactions: Herbst et al. 1993; H_3^+ + e: Smith & Spañel 1993; sulfur chemistry: Pineau des Forêts et al. 1993). We also checked our reaction network with that of the UMIST group (Bennet 1988; Millar et al. 1991, and references therein) and found only minor differences. The largest discrepancy occurred for the O + H^+ charge transfer reaction, for which we have adopted a fit to the rate coefficients given by Chambaud et al. (1980).

The chemical network includes 24 elements, and isotopes of H, C and O (see Table 2). The fact that many metals are included separately instead of just a few "canonical metals" is important, since deep inside the cloud the metals dominate the ionization balance, and differences in ionization potential become important. Charge transfer with large molecules, such as PAHs, is taken into account explicitly. The isotopes are treated separately because of isotope selective reactions due to small differences in binding energy, and, in the case of CO, because the main isotope will become self-shielding closer to the edge than the other isotopes. Note also that ^{13}C and $^{13}C^+$ are sufficiently abundant at the edge to be non-negligible reaction partners with other species. The network includes 1549 reactions among 215 species. The only grain surface reaction included is the formation of H_2 and HD. All observed molecules are included in the network, except the more complex CH_3OH, CH_3CN, HC_3N and HNCO molecules, for which only upper limits were obtained.

Our model includes ultraviolet line and continuum photodissociation cross sections based on the literature summarized by van Dishoeck (1988). These are used in combination with the input radiation field and the shielding to compute the actual photodissociation and photoionization rates at each depth. Shielding by dust grains is incorporated using the grain model of Roberge et al. (1991). The grains are described by their scattering function g_λ, albedo ϖ_λ and the extinction curve $A_\lambda/A_{\rm V}$ at a number of wavelengths in the range 912-10,000 Å. Self-shielding and mutual shielding of H_2 and CO (and isotopes), as described in van Dishoeck & Black (1986, 1988), have been incorporated in our model. Shielding of carbon photoionization by ultraviolet lines of H_2 is also included. Compared with the earlier work of van Dishoeck & Black (1988), the maximum amount of shielding has been limited to 50% rather than 90%.

Care has to be taken in applying this model to a PDR like IC 63, since the density and the ultraviolet flux are much higher than in a translucent cloud. Therefore other reactions may become important. At the outside the flux is high and photoreactions will drive the chemistry, but deeper in the cloud the molecules and atoms become shielded from ultraviolet radiation and cosmic rays become the dominant source of ionization. Tests have shown that the program and model work well for PDRs up to a visual extinction of about 20 mag, which is certainly sufficient for IC 63.

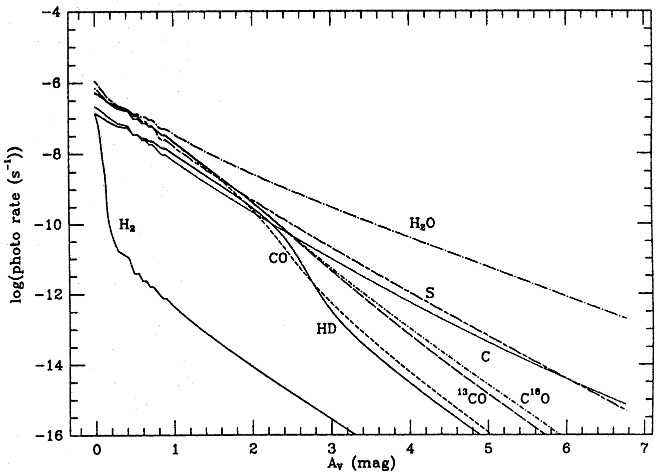

Fig. 4. Important photodissociation and photoionization rates as functions of depth into the cloud. Parameters are those of model 1 of Table 3

5.2. *Elemental abundances and depletions*

The elemental abundances used in our model are the solar abundances depleted by a certain factor. Different conventions are used in the literature to indicate the depletion of an element. We use the convention that when 60 % of the oxygen is in the gas phase, δO = 0.60. The remainder of the atoms is supposed to be in grains or, in the case of carbon, large molecules such as PAHs.

Since C^+, C and CO have all been observed in IC 63 (paper III), the total amount of gas-phase carbon is well constrained. It is found that only 13 ± 4 % of the solar carbon abundance is present in the gas-phase. Having fixed the carbon depletion, the other depletions can be constrained to fit the observed abundances of various molecules, e.g. CN, HCN and N_2H^+ are used to infer the nitrogen depletion. The gas-phase fraction of oxygen is not well determined from observations, but it must be higher than $\approx$ 30 % to provide sufficient cooling to get the temperature down to the observed value of about 50 K (see below).

Since the inferred depletions of carbon and nitrogen in IC 63 turn out to be close to one third of the depletions observed in ζ Oph (Cardelli et al. 1993; Savage et al. 1992), we assume that the same holds for other elements for which we do not have any observational constraints in IC 63. The only exception is sulfur, for which the depletion can be constrained from the observations of CS, and the upper limits on SO and SO_2. It is found that the sulfur must be quite depleted; only $\approx$ 3.5 % is in the gas phase instead of $\approx$ 50 % found in ζ Oph. Table 2 lists

Table 2. Assumed elemental abundances

Element	Solar Abundance[a]	Gas-phase fraction		
		ζ Oph [c]	model 1	model 6
H	1.0	1.0	1.0	1.0
D	1.5×10^{-5}	...	...	...
He	7.5×10^{-2}	1.0	1.0	1.0
C	4.0×10^{-4} [b]	0.33	0.13	0.13
^{13}C	7.8×10^{-6}	...	...	...
O	8.3×10^{-4}	0.35	0.60	0.60
^{18}O	1.7×10^{-6}	...	...	...
N	1.0×10^{-4}	0.77	0.25	0.25
Cl	1.1×10^{-7}	1.0	0.40	0.40
S	1.7×10^{-5}	0.49	0.035	0.035
Si	4.3×10^{-5}	0.019	0.0063	0.0019
P	2.8×10^{-7}	0.078	0.026	0.0078
Na	2.1×10^{-6}	0.36	0.12	0.036
Li	2.2×10^{-9}	0.16	0.053	0.016
Ca	2.2×10^{-6}	0.0027	0.0009	0.00027
Mg	4.2×10^{-5}	0.12	0.04	0.012
Fe	4.3×10^{-5}	0.0075	0.0025	0.00075
Mn	2.6×10^{-7}	0.059	0.0197	0.0059
Al	3.1×10^{-6}	0.0025	0.00083	0.00025
K	1.3×10^{-7}	0.078	0.026	0.0078
Ti	1.2×10^{-7}	0.0019	0.00063	0.00019
Cr	4.4×10^{-7}	0.03	0.01	0.003
Ni	1.7×10^{-6}	0.0058	0.00193	0.00058
Zn	4.0×10^{-8}	0.36	0.12	0.036
Rb	4.0×10^{-10}	0.18	0.06	0.018
Co	7.9×10^{-8}	...	0.06	0.018

[a] from Anders & Grevesse (1989), unless otherwise indicated; [b] Grevesse et al. (1991); [c] Cardelli et al. (1993), Savage et al. (1992), Lepp et al. (1988).

the cosmic abundances and depletions used for the models. We assume isotope ratios [^{12}C]/[^{13}C] = 60 and [^{16}O]/[^{18}O] = 500 for C and O in all forms. In our models we take 10 % of the gas-phase carbon in the form of PAHs.

5.3. Heating and cooling processes

The chemistry in a PDR is intimately coupled with the heating and cooling balance. The cooling occurs primarily through the emission lines of the atoms and molecules in the cloud, and is thus sensitive to the chemical composition. On the other hand, many chemical reaction rates are temperature dependent. Therefore, chemistry and temperature must be iterated together.

Cooling takes place through atomic fine structure lines of O, C, C$^+$ and molecular rotational lines (mainly CO). In the model, the coolants are excited by collisions and through ultraviolet absorption lines, as well as through absorption and emission in the cosmic background radiation field. A mean escape probability method was adopted to calculate the efficiency of these cooling lines, with the same algorithm as used in Paper I to analyse the observations. The efficiency of the cooling lines, in particular the [OI] 63μm line, can be affected by excitation by far-infrared radiation from dust. Test calculations show however, that this process is negligible for the case of IC 63.

The heating processes included in the model are the photoelectric effect, heating by cosmic rays, collisional de-excitation of vibrationally excited H_2 and chemical heating, which includes heating by formation and destruction of H_2. The photoelectric effect involves dust grains and large molecules such as PAHs. Since the probability that the photoelectrically released electron can escape the grain or molecule is inversely proportional to the size of the particle, small grains and large molecules dominate in this heating mechanism, especially at the edge (Lepp & Dalgarno 1988; Verstraete et al. 1990). Our model follows the treatment of Bakes & Tielens (1994), which takes the size and charge distribution of the PAHs into account. Classical grains, larger than 100 Å, are treated according to de Jong (1977). Deeper into the cloud, cosmic ray heating will become the most important heating mechanism.

Exoergic chemical reactions also contribute to the heating of the cloud, but in most cases this contribution is negligible. The most important exception is the formation of molecular hydrogen on grains (Tielens & Hollenbach 1985). Photodissociation of H_2 and photoionization of atomic carbon are included as heating sources as well, since the products of these reactions will generally have some of the excess energy (Stephens & Dalgarno 1972). Other sources of chemical heating that are included are dissociative recombination of the most abundant ions H_3^+, H_3O^+ and HCO$^+$, and destruction of H_2 and CO by He$^+$ ions.

6. Results of one-dimensional models

Chemical calculations have been performed for the IC 63 nebula, using the physical parameters summarized in Sect. 2: $n_{\rm H} = (10 \pm 4) \times 10^4\,{\rm cm}^{-3}$ (corresponding to $n({\rm H_2}) = (5 \pm 2) \times 10^4\,{\rm cm}^{-3}$, not including the small contribution of atomic hydrogen), $N({\rm H_2}) = (5 \pm 2) \times 10^{21}\,{\rm cm}^{-2}$, $A_{\rm V} = (6.7 \pm 2.3)$ magnitudes. These parameters were allowed to vary within the errors to obtain the best possible fit to the chemistry. The temperature was not included as a parameter, since it is calculated from the heating and cooling balance. It can therefore be used as an additional constraint on the model. The adopted radiation field is the measured IUE spectrum of γ Cas, as described in Sect. 3. Some model calculations with the other radiation fields shown in Fig. 2 were performed as well.

In the following the depth dependences of the abundances and the sensitivities to the parameters are discussed in more detail. The best fit to the observed column densities is obtained with $n_{\rm H} = 1 \times 10^5\,{\rm cm}^{-3}$, $N({\rm H_2}) = 5 \times 10^{21}\,{\rm cm}^{-2}$, $\zeta = 5 \times 10^{-17}\,{\rm s}^{-1}$ (model 1 in Table 3). It is seen that in most cases the agreement is of order a factor of three or better, the main exception being the sulfur-bearing molecules.

6.1. Depth dependence of abundances

The depth dependences of various species are illustrated in Figs. 5 a-l. In the models, several regions can be identified, each characterized by a different chemistry and by different dominant constituents (Sternberg & Dalgarno 1995). The outer part of

Table 3. Column densities (in cm^{-2}) from model calculations[a]

Model	1	2	3	4	5	6	7	Observed
$n_H(cm^{-3})$	1 (5)	7 (4)	1 (5)	1 (5)	1 (5)	1 (5)	1 (5)	...
$\zeta(s^{-1})$	5 (-17)	5 (-17)	2 (-16)	5 (-17)	5 (-17)	5 (-17)	5 (-17)	...
δC	0.13	0.13	0.13	0.13	0.25	0.13	0.13	...
δO	0.60	0.60	0.60	0.40	0.60	0.60	0.60	...
$\delta M/\delta M(\zeta$ Oph)	0.33	0.33	0.33	0.33	0.33	0.10	0.33	...
H_2 [b]	5.0 (21)	5.0 (21)	5.0 (21)	5.0 (21)	5.0 (21)	5.0 (21)	4.0 (21)	5.0 (21)
A_V (mag)	6.79	6.88	6.79	6.79	6.79	6.79	5.51	6.7
H	5.6 (20)	6.9 (20)	5.6 (20)	5.5 (20)	5.8 (20)	5.6 (20)	5.5 (20)	≈4.0 (20)
C	6.8 (16)	6.4 (16)	6.3 (16)	7.1 (16)	1.3 (17)	6.8 (16)	6.7 (16)	3.7 (16)
C^+	1.3 (17)	1.4 (17)	1.3 (17)	1.3 (16)	2.6 (17)	1.3 (17)	1.3 (17)	2.0 (17)
CO	3.2 (17)	3.2 (17)	3.3 (17)	3.2 (17)	7.0 (17)	3.3 (17)	2.3 (17)	3.0 (17)
^{13}CO	5.2 (15)	5.3 (15)	5.3 (15)	5.2 (15)	1.1 (16)	5.2 (15)	3.6 (15)	3.9 (15)
$C^{18}O$	2.7 (14)	2.9 (14)	3.6 (14)	2.7 (14)	5.6 (14)	2.7 (14)	1.1 (14)	5.0 (14)
CS	1.1 (13)	1.1 (13)	1.4 (13)	2.0 (13)	2.7 (13)	1.1 (13)	2.8 (12)	9.5 (12)
CN	2.6 (13)	2.8 (13)	3.3 (13)	3.9 (13)	5.1 (13)	2.6 (13)	2.4 (13)	2.7 (13)
HCN	1.4 (13)	1.6 (13)	2.6 (13)	1.7 (13)	1.3 (13)	1.4 (13)	2.7 (12)	4.0 (13)
HNC	7.1 (12)	7.7 (12)	1.3 (13)	8.5 (12)	6.4 (12)	7.1 (12)	1.3 (12)	1.1 (13)
HCO^+	2.0 (12)	2.2 (12)	6.6 (12)	2.6 (12)	3.4 (12)	2.0 (12)	7.6 (11)	8.0 (12)
H_2CO	8.6 (12)	9.4 (12)	1.2 (13)	1.4 (13)	1.1 (13)	8.6 (12)	3.5 (12)	5.0 (12)
C_2H	4.6 (13)	4.3 (13)	4.6 (13)	6.0 (13)	1.0 (14)	4.6 (13)	4.5 (13)	1.8 (13)
N_2H^+	2.0 (11)	2.4 (11)	9.9 (11)	3.0 (11)	1.5 (11)	2.0 (11)	5.5 (10)	2.9 (11)
H_2S	6.8 (11)	7.8 (11)	1.6 (12)	1.2 (12)	7.0 (11)	6.8 (11)	4.6 (10)	7.3 (12)
SO	9.3 (13)	1.1 (14)	2.8 (14)	1.2 (14)	8.2 (13)	9.3 (13)	6.3 (12)	<5.0 (12)
SO_2	7.8 (12)	1.1 (13)	9.7 (13)	1.4 (13)	6.2 (12)	7.8 (12)	4.5 (10)	<1.5 (13)
O	4.9 (18)	4.9 (18)	4.6 (18)	3.1 (18)	4.5 (18)	4.9 (18)	4.1 (18)	...
O_2	6.8 (16)	7.9 (16)	2.0 (17)	5.7 (16)	5.5 (16)	6.8 (16)	6.4 (15)	...
OH	3.5 (13)	4.9 (13)	1.5 (14)	4.6 (13)	3.1 (13)	3.5 (13)	2.4 (13)	...
H_2O	2.2 (16)	2.5 (16)	3.8 (16)	1.6 (16)	1.7 (16)	2.2 (16)	3.6 (15)	...
CH	1.4 (14)	1.3 (14)	1.4 (14)	1.6 (14)	2.2 (14)	1.4 (14)	1.4 (14)	...
CH_2	7.2 (13)	7.1 (13)	7.2 (13)	8.4 (13)	1.1 (14)	7.2 (13)	7.3 (13)	...
NH	3.0 (11)	4.3 (11)	1.7 (11)	6.0 (11)	2.3 (11)	3.0 (11)	1.7 (11)	...
NH_2	1.5 (14)	1.7 (14)	6.9 (14)	1.8 (14)	1.0 (14)	1.5 (14)	1.4 (13)	...
NH_3	1.4 (14)	1.6 (14)	3.4 (14)	1.6 (14)	9.1 (13)	1.4 (14)	1.7 (13)	...

[a] In all models, $\delta N = 0.25$, $\delta S = 0.035$, and the radiation field is taken to be that derived from IUE observations.
[b] Fixed to set the total size of the cloud.

the cloud, up to $A_V \approx 1.5$ mag, is the $C^+ \rightarrow C$ conversion zone. Most elements are still in atomic form, with the exception of hydrogen, which is already molecular. Subsequently around $A_V = 2$ mag the "radical region" occurs. In this zone the chemistry is dominated by simple, mostly diatomic, radicals like CH, CH_2, CN and OH. Carbon is being converted from C to CO in this region, but ionized carbon is still important.

In the zone from $A_V \approx 3$ to $A_V \approx 5$ mag the conversion to more complex molecules takes place. The electron abundance drops considerably. Photodissociation and photoionization are no longer important chemical reactions; their role as dominant destruction processes is taken over by oxygen, which is for the main part still in atomic form. This region will therefore be denoted as the "atomic O" region. Finally in the deepest part of the cloud, $A_V \gtrsim 5$ mag, oxygen is converted into O_2 and H_2O, and dark cloud chemistry has been reached.

6.1.1. C^+, C and CO

At the outer edge of the PDR, most of the carbon is ionized due to the efficient ionization by photons longward of 912 Å. Then, at $A_V \approx 2$ mag, most of the carbon becomes neutral since the ionizing photons are absorbed by dust and H_2 before reaching this depth. As can be seen in Fig. 5b, this zone is very narrow, since neutral atomic carbon is rapidly converted into CO. This happens at about the same depth, since the CO photodissociation and carbon photoionization require photons in the same part of the spectrum. Actually, in some of our models, neutral atomic carbon is never the dominant form of carbon; CO immediately takes over. The isotopes of CO reach their peaks somewhat deeper into the cloud, since they do not become self-shielding as quickly as the main isotope.

Isotope-selective photodissociation causes the $^{12}CO/^{13}CO$ column density ratio to be somewhat higher than the overall

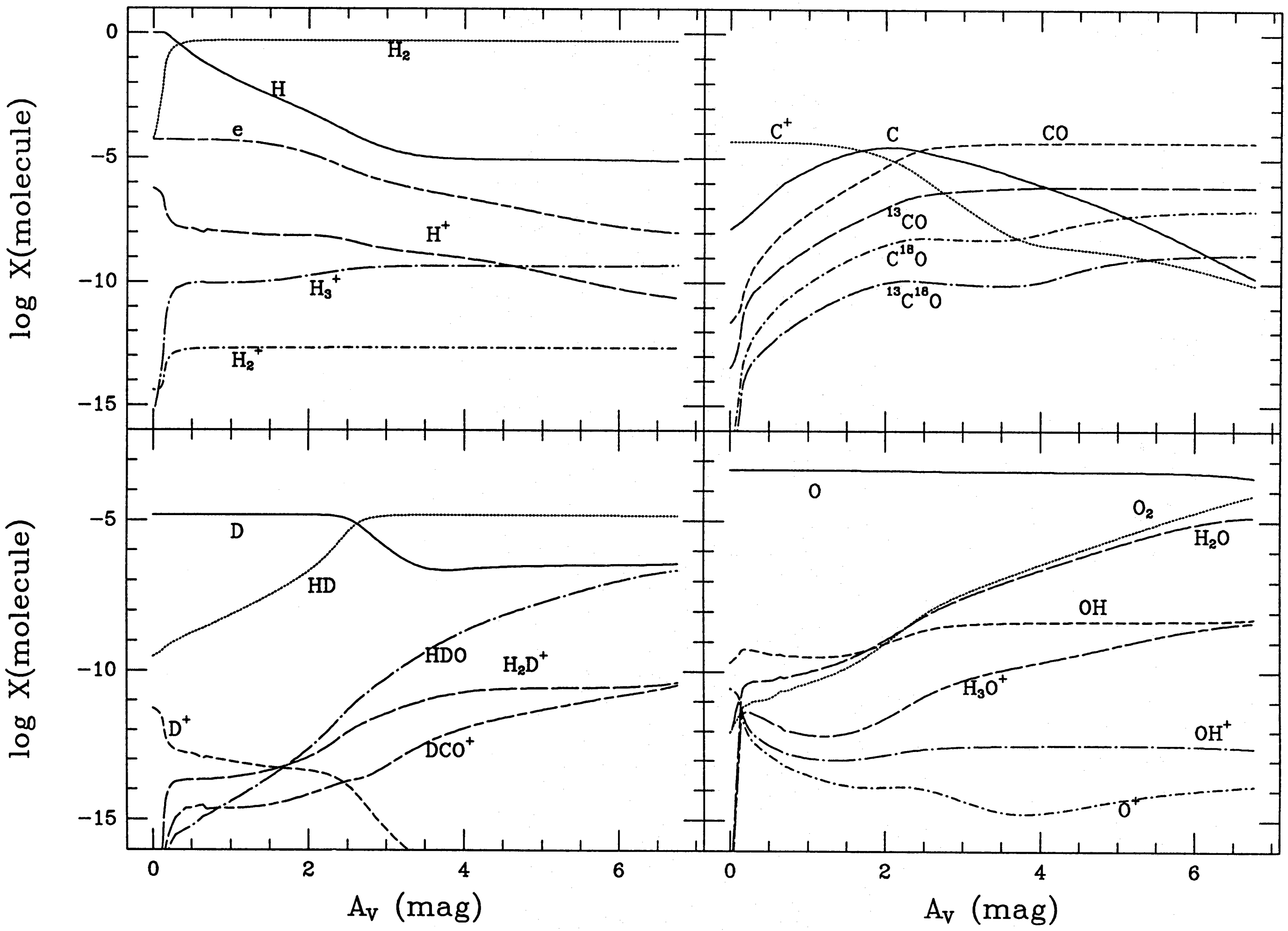

Fig. 5a-d. Abundances of selected species with respect to H_2 as functions of depth into the cloud. Parameters are those of model 1 of Table 3

$[^{12}C]/[^{13}C]$ ratio: 63 instead of the adopted ratio of 60. More significant is the deviation in the CO/$C^{18}O$ column density ratio, which is 1100 instead of the isotope ratio $[^{16}O]/[^{18}O] = 500$. This starts to become important at $A_V \gtrsim 2$, where the photodissociation rates of the isotopomers start to differ (see Fig. 4). At this depth, the abundances of C^+ and $^{13}C^+$ are already low, so the exchange reaction

$$^{13}C^+ + {}^{12}CO \rightarrow {}^{12}C^+ + {}^{13}CO \quad (+36\,K) \tag{2}$$

is not very important. Also, the temperature in this region is still above 40 K. The isotopomer ratio is then fixed at $A_V \approx 4$ mag, since the dominant removal process for CO at that depth becomes the reaction with He^+, which has the same reaction rate for all isotopic forms.

6.1.2. Carbon hydrides

The abundances of the carbon hydrides and their ions rise rapidly at $A_V \lesssim 1$ mag. Their formation is initiated by the reaction

$$C^+ + H_2 \rightarrow CH_2^+ + h\nu\,, \tag{3}$$

and thus the carbon hydrides are formed in large amounts where H_2 and C^+ coexist. Therefore these molecules reach their peak abundance in the "radical region". Deeper into the cloud, carbon is converted to C and CO, and this formation path is closed. Also, neutral-neutral reactions become important in their destruction, most noticeably:

$$\begin{aligned} &CH_2 + O \rightarrow CO + H + H \\ &CH_3 + O \rightarrow H_2CO + H \end{aligned} \tag{4}$$

This has as the result that the decrease in the abundances of the unsaturated carbon hydrides is even steeper than that of C^+ for $A_V > 2$ mag.

There is no corresponding reaction between CH_4 and atomic oxygen, since this process would be endoergic. Therefore the abundances of CH, CH_2 and CH_3 and their ions drop by 2 to 4 orders of magnitude at large A_V, whereas CH_4 stays at approximately the same level.

6.1.3. Carbon chains

The depth distribution of carbon chain molecules is well represented by C_2H in Fig. 5e. They all peak at about the same depth as neutral atomic carbon, $A_V \approx 2$ mag, which is not immediately obvious, since there is no direct route from neutral carbon

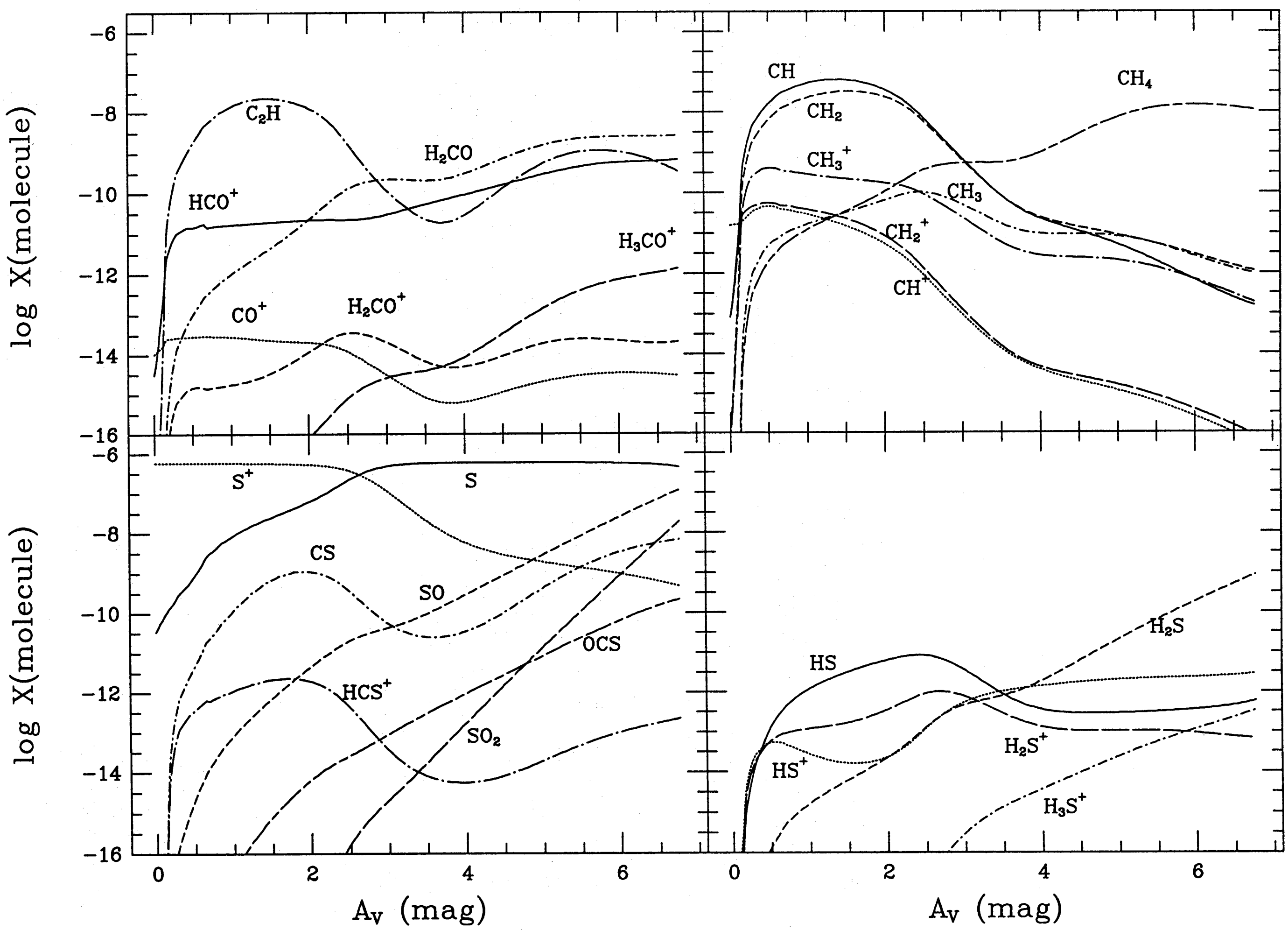

Fig. 5e-h. Abundances of selected species with respect to H_2 as functions of depth into the cloud. Parameters are those of model 1 of Table 3

to the carbon chains. This can be explained, however, by their main formation route (Suzuki et al. 1992):

$$\begin{aligned} C^+ + CH_2 &\rightarrow C_2H^+ + H \\ C^+ + CH &\rightarrow C_2^+ + H \\ C_2^+ + H_2 &\rightarrow C_2H^+ + H \\ C_2H^+ + H_2 &\rightarrow C_2H_2^+ + H \\ C_2H_2^+ + e &\rightarrow C_2H \end{aligned} \qquad (5)$$

and similar reactions for other carbon chains. Therefore, carbon chains form mainly in the "radical region", where both CH_x and C^+ are abundant, which is just the same region where neutral atomic carbon reaches its peak. For the longer carbon chains there are additional routes to include neutral carbon directly, such as:

$$C_2H_2^+ + C \rightarrow C_3H^+ + H \quad . \qquad (6)$$

Photodissociation and reactions with atomic oxygen are the main destruction routes of the carbon chain molecules.

6.1.4. Oxygen-bearing molecules

Only very few oxygen-bearing molecules have been observed in IC 63. The model predicts that most of the oxygen remains in atomic form throughout the cloud. Approximately 10 % of the oxygen is in the form of molecules, the most important being CO, O_2 and H_2O.

Oxygen cannot be ionized by the photons that are present inside the PDR, and so oxygen is in its neutral atomic form even in the outer layers of the cloud. In the outer part, the oxygen chemistry is initiated by the reaction

$$O + H^+ \rightarrow O^+ + H \quad . \qquad (7)$$

The rate coefficient of this important reaction was computed by Chambaud et al. (1980) and has a strong temperature dependence of $e^{-227/T}$, so that it becomes less important deeper inside where the reaction

$$O + H_3^+ \rightarrow OH^+ + H_2 \qquad (8)$$

takes over. The formation of OH and H_2O proceeds through the reactions

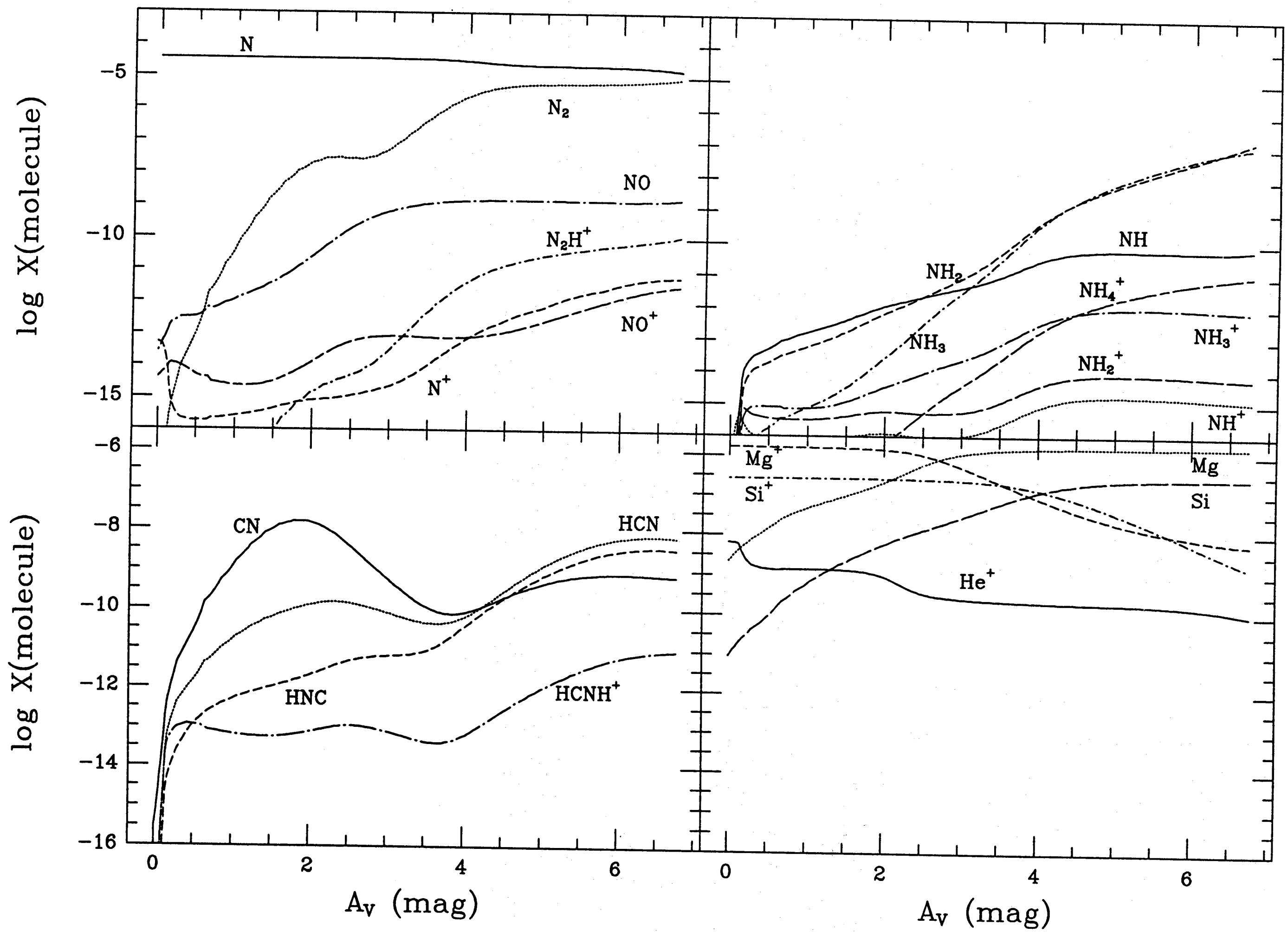

Fig. 5i-l. Abundances of selected species with respect to H_2 as functions of depth into the cloud. Parameters are those of model 1 of Table 3

$$\begin{aligned} O^+ + H_2 &\rightarrow OH^+ + H \\ OH^+ + H_2 &\rightarrow H_2O^+ + H \\ H_2O^+ + H_2 &\rightarrow H_3O^+ + H \\ H_3O^+ + e &\rightarrow H_2O + H \\ &\rightarrow OH + H_2 \quad . \end{aligned} \tag{9}$$

For this last reaction step the branching ratio is taken to be 65 % in favor of OH formation (Herd et al. 1990). At the edge, OH is mainly removed by photodissociation and reactions with C^+. Deeper inside it is both formed and removed by reactions involving atomic oxygen, so that its abundance remains approximately constant throughout the cloud. Water is mainly removed by photodissociation and not by atomic oxygen, so deeper into the cloud the abundance of H_2O keeps rising when the photorates drop.

Formation of O_2 takes place through the reaction

$$OH + O \rightarrow O_2 + H \quad , \tag{10}$$

which is the dominant removal reaction for OH at larger depths. Molecular oxygen can most easily be destroyed by photodissociation. Destruction of OH by atomic or ionized carbon, leading to CO and CO^+ respectively, plays a less important role, partially because of the low carbon abundance in our models.

6.1.5. Carbon-oxygen molecules

At the edge of the cloud, HCO^+ is formed primarily by the reactions

$$\begin{aligned} C^+ + OH &\rightarrow CO^+ + H \\ CO^+ + H_2 &\rightarrow HCO^+ + H \\ CH + O &\rightarrow HCO^+ + e \\ CH_2^+ + O &\rightarrow HCO^+ + H \quad . \end{aligned} \tag{11}$$

Therefore, HCO^+ reaches a small peak at the depth where the carbohydrides peak. Then, at $A_V \gtrsim 1.5$, the abundance of the HCO^+ ion follows the CO abundance since its primary formation route has now become

$$CO + H_3^+ \rightarrow HCO^+ + H_2 \quad . \tag{12}$$

At this same depth the electron fraction drops, thus decreasing the HCO^+ destruction through recombination. Even so, recombination stays the most important destruction mechanism for

HCO^+. Only in the deepest part of the cloud, do proton transfer reactions like

$$HCO^+ + H_2O \rightarrow CO + H_3O^+ \tag{13}$$

become important for the removal of HCO^+.

Formaldehyde, H_2CO, is mainly formed through the reaction

$$CH_3 + O \rightarrow H_2CO + H \tag{14}$$

thus causing an abundance peak close to $A_V = 2$ mag. The most important removal reaction for this molecule is photodissociation, and since this rate drops off quite steeply, it compensates for the decrease in the formation rate when the CH_3 abundance drops, causing the formaldehyde abundance to stay almost constant over the inner part of the cloud. The computed H_2CO column density using this pure gas-phase chemistry scheme agrees well with observations; no photo-processing of the molecule in icy grain mantles (cf. Shalabiea & Greenberg 1994) appears required.

6.1.6. Nitrogen-bearing molecules

Most of the nitrogen is in the form of N and N_2, where N_2 only starts to become significant in the center of the cloud. Nitrogen hydrides, NH, NH_2, NH_3 are formed through the ions NH_x^+. Their formation is therefore initiated by

$$N^+ + H_2 \rightarrow NH^+ + H \tag{15}$$

which requires ionized nitrogen, a species that is mainly formed by cosmic ray ionization of neutral atomic nitrogen or through the reaction between N_2 and He^+. We adopted a rate coefficient of $1 \times 10^{-9}\ \mathrm{cm^3\,s^{-1}}$ for reaction (15) according to Le Bourlot et al. (1993). Since the abundance of H_2 and the cosmic ray ionization rate are almost constant over the cloud, the formation rate of the NH_x species is also constant. The destruction of NH_2 and NH_3 is mainly due to photodissociation, which drops off rapidly at higher depth into the cloud, and as a consequence the abundances of these species continue to rise. The NH radical on the other hand, is efficiently removed through

$$NH + O \rightarrow OH + N \tag{16}$$

in the atomic oxygen region, and this reaction compensates for the decrease in the photodissociation rate, causing the NH abundance to stay almost constant for $A_V \gtrsim 3$ mag. The corresponding reaction involving NH_2

$$NH_2 + O \rightarrow NH + OH \tag{17}$$

is an order of magnitude less efficient (Mitchell & Deveau 1983). The computed NH_2 column density is comparable to that observed by van Dishoeck et al. (1993) in the low density envelope toward Sgr B2, which is thought to have similar physical parameters as the IC 63 cloud.

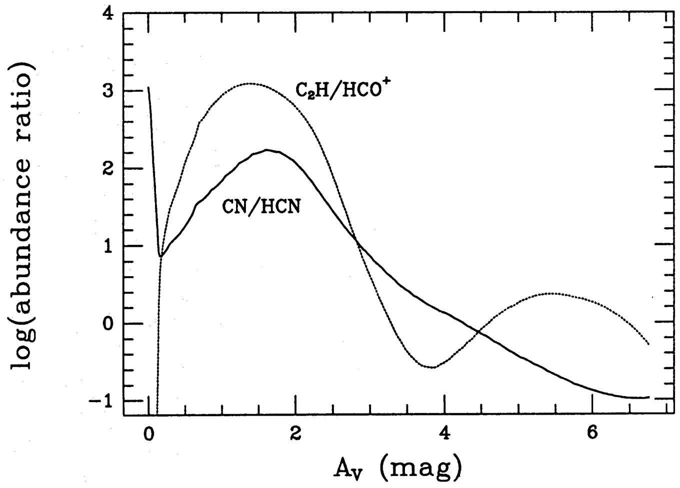

Fig. 6. Depth dependence of the CN/HCN and C_2H/HCO^+ ratios

The most important observed nitrogen-bearing molecules are CN, HCN, HNC and N_2H^+. The abundance ratio between CN and HCN shows large variations with depth into the cloud (see Fig. 6), whereas HNC has approximately the same distribution as HCN. The CN abundance peaks around $A_V \approx 2$ mag in the "radical region", after which it falls off by about 2 orders of magnitude. This peak is mainly caused by the reactions (Federman et al. 1984)

$$\begin{aligned} N + C_2 &\rightarrow CN + C \\ N + CH &\rightarrow CN + H \end{aligned} \tag{18}$$

and to a lesser extent

$$C + NH \rightarrow CN + H \quad , \tag{19}$$

which explains why this peak coincides with the carbon chain and carbon hydride peaks.

Deeper inside the cloud, CN and HCN (and HNC) form from dissociative recombination of the $HCNH^+$ ion:

$$\begin{aligned} HCNH^+ + e &\rightarrow CN + H + H \\ &\rightarrow HCN + H \\ &\rightarrow HNC + H \quad . \end{aligned} \tag{20}$$

In our model we have assumed equal probability for these reactions, so in this part of the cloud CN, HCN and HNC form in approximately equal amounts. CN however, can be destroyed by atomic oxygen, whereas HCN cannot, and therefore the CN abundance becomes lower than that of HCN in the "atomic oxygen region".

Differences in abundance between HCN and HNC are caused by three mechanisms. First, HNC may be converted to the more stable form HCN by temperature-dependent auto-isomerization. The nature of this mechanism is not yet known and it probably has a large energy barrier. We have not included it in our model. Second, HNC can be selectively removed in warm clouds compared to cold clouds. This is suggested by observations of cold clouds, where HCN/HNC ≈ 1, compared with warm clouds, where the ratio is $\gtrsim 100$ (see Irvine et al. 1985 and references therein). Schilke et al. (1992) suggest that the reaction between HNC and O can occur, but not between HCN and O. In our calculations we follow this model with their suggested energy barrier of 200 K for the HNC + O reaction. A third mechanism included in our reaction network is found in the difference in two minor formation routes: HCN can be formed from N + CH_2, whereas HNC can be formed from C + NH_2, so the difference in abundance between these reactants can cause differences between HCN and HNC. This is just a minor effect compared with the selective reaction with atomic oxygen integrated over the whole cloud. However, in the "radical region" the CH_2 abundance peaks, whereas that of NH_2 does not. This is clearly reflected in the abundances of HCN and HNC, in that the former is enhanced by more than an order of magnitude compared to the latter.

Note that most of the CN is present in a part of the cloud where the abundance of free electrons is rather large, $X(\mathrm{e}) \approx 3 \times 10^{-5}$, but that most of the HCN and HNC is located in the part where the electron abundance is as low as 1×10^{-6} – 1×10^{-8}. This justifies the assumption that the observed column densities for these species are those derived in Paper I for a low electron fraction.

6.1.7. Sulfur-bearing molecules

Most of the sulfur is in ionized form at the outer part of the cloud; the transition from S^+ to S takes place between $A_V \approx 2$ and 4 mag. The most important sulfur-bearing molecules in our chemical network are CS, SO and SO_2.

Molecules like CS, CS^+ and HCS^+ show a peak at $A_V \approx 2$ mag, due to the reaction

$$S^+ + CH \rightarrow CS^+ + H \tag{21}$$

followed by

$$\begin{aligned} CS^+ + H_2 &\rightarrow HCS^+ + H \\ HCS^+ + e &\rightarrow CS + H\,. \end{aligned} \tag{22}$$

The peak of CS in the radical region is therefore due to the peak in CH discussed above, which occurs at about this same depth. At greater depth, the abundances of CS and related molecules drop, but they start to rise again at $A_V \approx 2.5$ mag, due to reactions involving SO and SO_2, e.g.:

$$SO + C^+ \rightarrow CS^+ + O\,. \tag{23}$$

CS is primarily destroyed by photodissociation and photoionization. The other important removal reaction at $A_V \gtrsim 5$ is

$$CS + H_3^+ \rightarrow HCS^+ + H_2 \tag{24}$$

but most of the HCS^+ formed by this reaction goes back to CS through Eq. 22. Destruction of CS by atomic oxygen is assumed to be inefficient at low temperatures; we adopt the rate coefficient published by Atkinson et al. (1989), which has an energy barrier of 760 K.

SO and SO_2 are not present at the edge of the cloud, but their abundances start to rise rapidly at $A_V \approx 2.5$ mag — the same depth where atomic sulfur becomes significant — due to the neutral-neutral reactions

$$\begin{aligned} S + O_2 &\rightarrow SO + O \\ S + OH &\rightarrow SO + H \\ HS + O &\rightarrow SO + H\,. \end{aligned} \tag{25}$$

For the first of these reactions, we have assumed an energy barrier of 265 K, as suggested by Pineau des Forêts et al. (1993), based on calculations of Craven & Murrell (1987). Most previous calculations (e.g. Prasad & Huntress 1982; Drdla et al. 1989; Sternberg & Dalgarno 1995) predicted that in the center of the cloud, most of the sulfur is converted into SO_2 and to a lesser extent SO. This is not in agreement with dark cloud and PDR observations, including our own. With the inclusion of the energy barrier in the S + O_2 reaction, this effect is not as strong in our model, although we still overproduce SO by nearly an order of magnitude. Even at the highest visual extinctions present in our model, the main destruction process for both SO and SO_2 is photodissociation.

In the outer part of the cloud, H_2S is formed through the reaction route:

$$\begin{aligned} S^+ + H_2 &\rightarrow H_2S^+ + h\nu \\ H_2S^+ + M &\rightarrow H_2S + M^+ \end{aligned} \tag{26}$$

where M stands for an arbitrary metal. An alternative route gains importance more towards the cloud center, since it starts from neutral atomic sulfur:

$$\begin{aligned} S + H_3^+ &\rightarrow HS^+ + H_2 \\ HS^+ + H_2 &\rightarrow H_3S^+ + h\nu \\ H_3S^+ + e &\rightarrow H_2S + H\quad. \end{aligned} \tag{27}$$

Both reaction paths involve a radiative association reaction, which is the slowest step. The amount of H_2S formed through these reactions is therefore quite low, much lower than the observed column density. Some other process not included in the current models, e.g. formation of H_2S on grains, may be responsible for its large abundance. H_2S is destroyed through photodissociation and the reaction with H_3^+ and HCO^+ which form H_3S^+, but most of the formed ions goes back to H_2S.

6.2. *Influence of density and total column density*

When a lower density is used (model 2, $n_H = 7 \times 10^4\,\mathrm{cm}^{-3}$), many reactions are less effective, especially recombination and ion-molecule reactions, resulting in larger column densities of atomic or ionized species. The transition to atomic form takes place deeper into the cloud. This is clearly seen from the models: both H and C^+ are enhanced by about 10–20 %, mostly at the expense of molecular hydrogen and neutral carbon, respectively. Since our modeling procedure integrates until a specified column density of molecular hydrogen has been reached, lowering the density has the effect of increasing the size of the cloud in order to obtain the same total H_2 column density. This enlargement of the cloud increases especially the extent of the "radical region". Molecules that peak in this region, such as CN and CS, have higher total column densities in the low density model. The carbon chain molecules, such as C_2H, are not enhanced, due to the decreased atomic carbon abundance. Molecules which are abundant both in the "radical region" and deeper into the cloud are not very sensitive to the density.

When a lower total column density is used (model 7, $N(H_2) = 4 \times 10^{21}$ cm^{-2}), the cloud gets smaller, but not much changes in the outer parts of the cloud. Molecules which have a high abundance in the dark cloud region, such as CS, HCN, H_2S, SO and SO_2, reach much lower column densities in this model.

6.3. *Cosmic ray ionization*

Increasing the cosmic ray ionization rate by a factor of 4 (model 3, $\zeta = 2 \times 10^{-16}$ s^{-1}) increases the amount of ions, and therefore enhances the ion-molecule chemistry. Ions like HCO^+ and N_2H^+ are enhanced by factors of about 3–5, and also molecules like OH, HCN and HNC are increased, since their formation is initiated by H_3^+ ions and cosmic ray ionization of atomic nitrogen. The enhancement in OH causes faster formation of many other molecules, including SO and SO_2; SO_2 increases more than linearly with the cosmic ray rate, since its formation includes two reactions involving OH. Decreasing the cosmic ray ionization rate to $\zeta = 1 \times 10^{-17}$ s^{-1} has the opposite effect of decreasing the abundances of these molecules. Other molecules are both formed and destroyed through reactions involving He^+ or H_3^+ ions, whose abundances are proportional to the cosmic ray ionization rate, so the abundances of these species are not enhanced in model 3.

6.4. *Depletion variations*

Changing the oxygen depletion has a large influence on the composition of the cloud. Model 4 shows the effect of lowering the gas-phase fraction of oxygen to $\delta O = 0.40$. Since reactions with atomic oxygen are the main destruction route for many radicals, e.g. CH_x and CN, such species are very sensitive to the amount of oxygen present in the gas-phase. In the case of CN, raising the oxygen gas-phase fraction to 90 % would lower the amount of CN by a factor of 2. Lowering the gas-phase oxygen to 40 %, as in model 4, increases the amount of CN by a factor of 1.5. Another concern is the cooling of the cloud. If the gas-phase fraction of oxygen were lower than approximately 0.30, then the cooling is insufficient to lower the temperature, because in our models the carbon abundance is also low. With such a low oxygen abundance, the temperature in the center of the cloud would still be as high as 60 K (see below). A justification for a low gas-phase fraction of oxygen relative to the solar abundance can be found in a recent publication by Meyer et al. (1994), who find that the interstellar O abundance toward two lightly reddened stars in Orion is only 40 % of solar.

Model 5 shows the results obtained with a higher gas phase abundance of carbon. The differences are as expected: increasing the amount of gas-phase carbon by a factor of 2 increases the column densities of most carbon-bearing molecules by almost this same factor. A molecule like C_2H however, is increased by a larger factor, although it does not scale exactly with the square of the gas-phase carbon abundance. This provides a good check on the inferred carbon depletion, since none of the models is able to compensate for such an increase in C_2H. From the observed C_2H column density it is found that the amount of gas-phase carbon must be around 0.08 times the total abundance, which is in good agreement with the value of 0.13 found from the observed amounts of C^+, C and CO. Molecules for which the dominant destruction route involves another carbon-bearing species, e.g. C^+, are less enhanced in model 5. Some are even less abundant in the case of a higher carbon abundance, such as HCN and HNC.

When the amount of gas-phase sulfur is increased, too much CS and SO is produced. Since these species scale almost linearly with the sulfur depletion. Therefore, our estimate of the sulfur depletion cannot be much higher than 0.04 in order to be consistent with the CS observations. The SO upper limit would even require a much lower gas-phase abundance of sulfur. Although the observed amount of H_2S could be reproduced if sulfur were essentially undepleted, this would greatly overproduce CS, SO and SO_2. The determination of the gas-phase fraction of sulfur from the observed CS abundance, however, depends heavily on the reactions that form and destroy CS, and in particular the destruction reaction between CS and atomic oxygen. We have used the value from Atkinson et al. (1989), who list it as $2.7 \times 10^{-10} e^{-760/T}$ cm^3 s^{-1}, i.e. with a rather high temperature barrier, so that this reaction never becomes dominant under the conditions in IC 63. If this reaction were a rapid neutral-neutral reaction instead, then the CS abundance might be reproduced with a relatively undepleted sulfur abundance, explaining the abundance of H_2S, but making the SO and SO_2 problem worse.

The depletions of the metals were argued to be approximately 0.33 times the ζ Oph values. A higher gas-phase fraction of metals will affect the column densities of ions like HCO^+ and N_2H^+, which are very sensitive to the ionization balance since they are destroyed by dissociative recombination with an electron. Actually, the calculated column densities of these molecular ions are somewhat low compared with observations, which might indicate that the gas-phase metal abundances should in fact be even lower. Model 6 of Table 3 shows such a model, in which the metals are depleted at 0.1 times the ζ Oph depletions (see Table 2 for the actual values). In this model HCO^+ is enhanced by a factor of 1.5.

6.5. *Radiation field*

Table 4 shows models with the same parameters as model 1 of Table 3, but using different radiation fields. The most important part of the spectrum is $\lambda \lesssim 1200$ Å, where the photodissociation of species like H_2, CO and CN takes place. Since the only available measurement at $\lambda < 1100$ Å is the broad-band mea-

1995A&A...302..223J

Table 4. Column densities (in cm^{-2}) from model calculations using different radiation fields[a]

Field	IUE	OAO-2	S2-68	Draine ×650	Mathis ×900	Observed
A_V (mag)	6.79	6.79	6.79	6.48	6.44	6.7
H_2 [b]	5.0 (21)	5.0 (21)	5.0 (21)	5.0 (21)	5.0 (21)	5.0 (21)
H	5.6 (20)	5.6 (20)	5.5 (20)	1.7 (20)	1.2 (20)	≈4.0 (20)
C	6.8 (16)	6.9 (16)	6.6 (16)	2.7 (16)	1.9 (16)	3.7 (16)
C^+	1.3 (17)	1.3 (17)	1.3 (17)	1.2 (17)	1.2 (17)	2.0 (17)
CO	3.2 (17)	3.2 (17)	3.2 (17)	3.5 (17)	3.5 (17)	3.0 (17)
^{13}CO	5.2 (15)	5.2 (15)	5.2 (15)	5.8 (15)	5.9 (15)	3.9 (15)
$C^{18}O$	2.7 (14)	2.6 (14)	2.7 (14)	2.4 (14)	2.5 (14)	5.0 (14)
CS	1.1 (13)	9.9 (12)	1.1 (13)	5.8 (12)	6.9 (12)	9.5 (12)
CN	2.6 (13)	2.4 (13)	2.5 (13)	2.1 (13)	2.7 (13)	2.7 (13)
HCN	1.4 (13)	1.3 (13)	1.3 (13)	8.8 (12)	9.5 (12)	4.0 (13)
HNC	7.1 (12)	6.4 (12)	6.6 (12)	4.4 (12)	4.7 (12)	1.1 (13)
HCO^+	2.0 (12)	1.9 (12)	1.9 (12)	1.5 (12)	1.5 (12)	8.0 (12)
H_2CO	8.6 (12)	7.8 (12)	8.4 (12)	5.7 (12)	5.7 (12)	5.0 (12)
C_2H	4.6 (13)	3.8 (13)	4.5 (13)	1.9 (13)	2.7 (13)	1.8 (13)
N_2H^+	2.0 (11)	1.8 (11)	1.9 (11)	1.4 (11)	1.4 (11)	2.9 (11)
H_2S	6.8 (11)	5.1 (11)	6.6 (11)	2.3 (11)	2.6 (11)	7.3 (12)
SO	9.3 (13)	7.4 (13)	8.9 (13)	3.4 (13)	3.7 (13)	<5.0 (12)
SO_2	7.8 (12)	4.6 (12)	7.0 (12)	9.7 (11)	1.2 (12)	<1.5 (13)
O	4.9 (18)	4.9 (18)	4.9 (18)	4.7 (18)	4.7 (18)	...
O_2	6.8 (16)	5.4 (16)	6.9 (16)	2.6 (16)	3.1 (16)	...
OH	3.5 (13)	3.4 (13)	3.5 (13)	3.3 (13)	3.3 (13)	...
H_2O	2.2 (16)	1.9 (16)	2.1 (16)	1.1 (16)	1.2 (16)	...
CH	1.4 (14)	1.3 (14)	1.2 (14)	8.3 (13)	1.1 (14)	...
CH_2	7.2 (13)	6.5 (13)	7.2 (13)	4.5 (13)	5.2 (13)	...
NH	3.0 (11)	2.9 (11)	3.0 (11)	3.0 (11)	3.1 (11)	...
NH_2	1.5 (14)	1.1 (14)	1.3 (14)	5.2 (13)	5.9 (13)	...
NH_3	1.4 (14)	1.1 (14)	1.3 (14)	6.4 (13)	7.1 (13)	...

[a] In all models, $\delta C= 0.13$, $\delta O= 0.60$, $\delta N= 0.25$, $\delta S= 0.035$, $\delta M = 0.33 \times \delta M(\zeta \text{ Oph})$, $n_H = 1 \times 10^5 cm^{-3}$, $\zeta = 5 \times 10^{-17} s^{-1}$.

[b] Fixed to set the total size of the cloud.

surement of Troy et al. (1975), the different γ Cas spectra used for Table 3 are identical in this wavelength range, and so the differences between these models are small. The scaled Draine (1978) and Mathis et al. (1983) fields are significantly lower in this wavelength range, resulting in less atomic hydrogen and carbon and more H_2 and CO. Note that more H_2 results in a lower total visual extinction, due to the way in which our code is set up. This lower A_V in turn causes column densities of species that peak at the center of the cloud to be lower, as can be seen with e.g. H_2CO. Because photo-processes are only important up to $A_V \approx 3$ mag, the overall effect is still small, except for species that live close to the edge of the cloud, such as atomic hydrogen and carbon.

6.6. Heating and cooling and the temperature structure

Figure 7 shows the most important heating and cooling rates as functions of depth. The resulting temperature structure is shown in Fig. 8. It can be seen that the temperature at the edge of the cloud is approximately 200 K, whereas the temperature in the cloud center in close to 10 K, as is the case in cold, dark clouds. At the edge the heating is dominated by the photoelectric effect on the grains. Also, H_2 formation and dissociation contribute significantly to the heating, but only up to $A_V \approx 0.2$ mag. Then, photoionization of PAHs becomes the second most important heating source. Finally, at $A_V \approx 5.7$ mag, all the heating rates induced by ultraviolet photons have dropped so low that cosmic ray heating becomes the dominant process.

The cooling at the edge of the cloud is dominated by atomic oxygen. Ionized carbon contributes only a few percent to the total cooling rate. This is partially due to the low carbon abundance used in our models. CO takes over as the most important coolant at $A_V \approx 2$ mag. The depletion of oxygen can be constrained from the cooling needed to get the bulk of the cloud at temperatures below 50 K. The gas-phase fraction of O should be at least 30 % because otherwise the cooling by atomic oxygen and CO is not efficient enough, and the temperature stays above 50 K even in the center of the cloud. An upper limit to the oxygen depletion cannot be found, since in the case that all the oxygen is in the gas phase, most of it will be converted into O_2 and this molecule does not contribute to the cooling. However, values of $\delta O > 0.8$ are unrealistic, since at least 20 % of

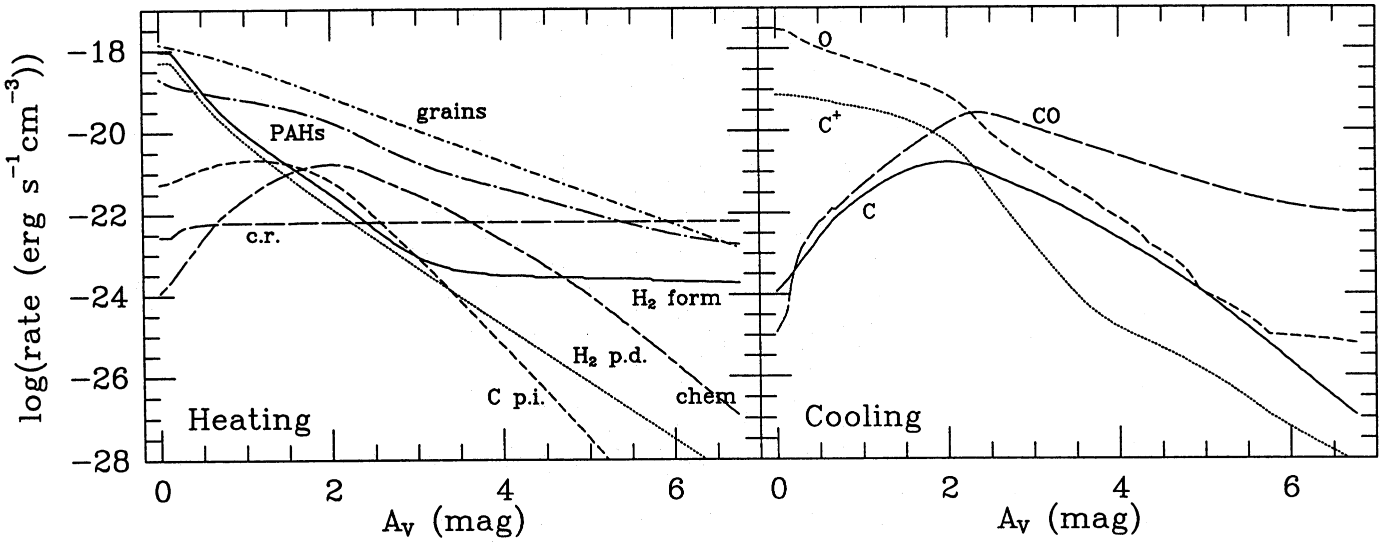

Fig. 7. Heating and cooling rates throughout the IC 63 nebula

Table 5. Column averaged temperatures $\langle T \rangle$ (K)

	model 1	model 4	model 5	two-dim.
edge	170	216	183	231
center	10	10	10	12
H_2	34	37	34	58
C^+	94	111	100	155
C	43	45	45	63
CO (thin)	18	18	18	19
CO (thick)	41	41	40	36
H_2CO	13	13	13	14

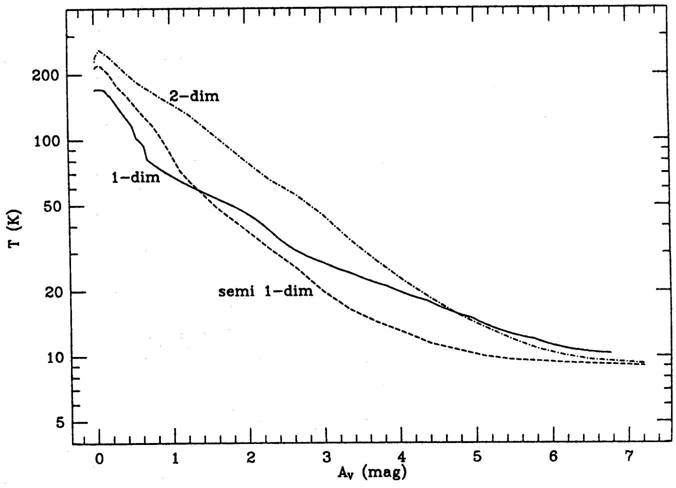

Fig. 8. Temperature of the cloud as a function of visual extinction. The solid curve is for model 1 of Table 3; the dash-dotted curve is the full two-dimensional model (T1), and the dashed curve is the semi one-dimensional model, both of which are described in Sect. 7

the oxygen is expected to be locked up in the silicate grains. Thus, the [CII] 158 μm line is never the dominant coolant in our models.

The resulting temperature structure and relative importance of the various heating and cooling mechanisms are consistent with the findings of Le Bourlot et al. (1993) when the differences in the model parameters are taken into account.

To compare the computed temperature profile with the temperature inferred from the observations the column averaged temperatures

$$\langle T \rangle_X = \frac{\int T(z) n(X,z) dz}{\int n(X,z) dz} \tag{28}$$

have been computed. The results for various species X that might function as temperature indicators are listed in Table 5. Most potential temperature indicators have optically thin lines, so the temperature they trace is the average temperature, weighted by the fractional density of the tracer at each depth step. Since CO is our main temperature indicator through its thermalized optically thick lines, the temperature integrated up to the $\tau = 1$ surface of the cloud in the CO lines has to be compared with the observations. This occurs at about $A_V = 2.5$ mag for the $2 \rightarrow 1$ line, and at about $A_V = 2.2$ mag for the $4 \rightarrow 3$ line (paper III). The temperature at these depths are 33 K and 41 K respectively for model 1, which is somewhat lower, but comparable to the value of (50 ± 20) K derived from the observations.

7. Two-dimensional models

In the one-dimensional models, the only dimension is the depth into the cloud, so these models treat the radiation field coming into the cloud from one side, and calculate the column density as seen from the other side. Since this geometry is clearly not correct, we also constructed two-dimensional models. These calculations are performed using the code described by Spaans (1995). This is an independent code, using a Monte Carlo method for the radiative transfer. It can be used with an arbitrary geometry, and the direction of the incident radiation field can be fully specified. This code uses A_V to constrain the total size of the cloud, instead of $N(H_2)$. A restricted chemical network, with only 663 reactions among 116 species, was used to speed up the calculations.

The adopted geometry is based on the CO $2 \rightarrow 1$ and $3 \rightarrow 2$ maps presented in paper I. A 200 by 200 point grid was used, resulting in a resolution of $\approx 0.25''$ or 3×10^{-4} pc. This geometry is shown in Fig. 9. The main contribution to the radiation field inside the cloud comes from photons from the direction of γ Cas, but photons scattered in other regions of the nebula may contribute significantly as well (see Fig. 9). The other model parameters such as density and elemental abundances are the same as in model 1 of Table 3. Three variations were used: model T1 of Table 6 uses the observed geometry in the plane of the sky, with radiation coming from the direction of γ Cas. Model T2 adds the general galactic radiation field incident on all sides of the cloud. The third model, T3, puts IC 63 a little further from the observer, using an angle of 30° between the plane of the sky and the line connecting IC 63 and γ Cas, thus increasing the distance between star and cloud, and decreasing the radiation field.

It can be seen from Fig. 8 that model T1 gives considerably higher temperatures than the one-dimensional modelin the largest part of the cloud. This is due to radiation penetrating the cloud from the sides and radiation scattered in different parts of the nebula, both of which effects are not present in the one-dimensional models. As a test, we have also performed a semi one-dimensional calculation with the two-dimensional code. In this model, the cloud is represented as a box with periodic boundary conditions, essentially turning it into a plane-parallel slab. This geometry causes the average pathlength and extinction for scattered radiation to be larger compared to the geometry adopted for IC 63 in the full two-dimensional model. It has the effect of lowering the temperature in the inside of the cloud, as can be seen in Fig. 8. It is clear that this semi one-dimensional model gives a temperature structure much closer to the one found in Sect. 5.6 from the one-dimensional models, as was to be expected. This shows that the geometry is quite important for understanding the temperature structure for this particular line of sight. The differences in the temperature structure found in the different two-dimensional models are small. The main difference between models T1 and T2 is that with the general interstellar radiation field included, the temperature increases to ≈ 25 K at the side furthest from γ Cas, but only in a small layer where $A_V \gtrsim 6$ mag.

This enhancement in temperature — and photo-rates — does not change the column densities by more than a few percent, and model T2 is therefore not listed in Table 6. The differences with model T3 are larger, and can be explained in terms of the lower radiation field.

For comparison of the two-dimensional models with the one-dimensional models and with the observed column densities, the molecular densities have been integrated over the shaded area shown in Fig. 9. This area is comparable to the telescope beam of $\approx 20''$. The resulting column densities for a number of important molecules are listed in Table 6 for the two-dimensional models described above, as well as for the semi one-dimensional case. These results are in good agreement with the one-dimensional models, although comparison is only possible for a limited number of molecules. Abundances of molecules which occur primarily in the "radical region" are reduced in model T3 due to the weaker radiation field and the lower atomic carbon abundance; this is clearly seen for CS and C_2H. The differences between models T1 and T2 are only a few percent, and model T2 is therefore not listed in Table 6.

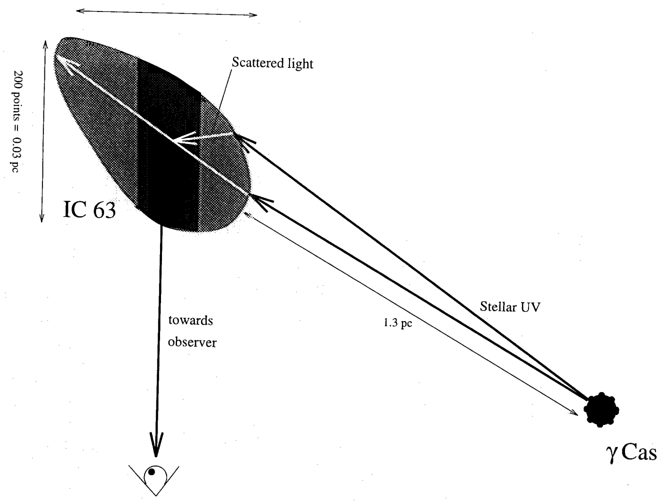

Fig. 9. Geometry used for the two-dimensional calculations

Note that the two-dimensional results are very sensitive to where this "beam" is placed over the model cloud. Figure 10 shows the column densities of the species C^+, C and CO with an infinitely small beam at different positions on a cross-cut along the white arrow in Fig. 9. It can be seen that as long as the beam is placed around the $(0'', 0'')$ position, the variations are not important, but closer to one of the edges the observed column densities become strong functions of the beam position.

The current two-dimensional models T1 and T2 cannot explain the extended C^+ and C emission at the tail of the cloud (paper III). However, a model like T3, but with a larger inclination with respect to the plane of the sky, could solve this problem. Another possible explanation would be the presence of a second "clump" at the position of the tail, not shielded by the main clump. Such a second clump could be suggested by the CO $3 \rightarrow 2$ map in paper I.

8. Comparison with other PDR models

Sternberg & Dalgarno (1995) recently published a PDR model for a somewhat denser cloud, $n_H = 1 \times 10^6\,\mathrm{cm}^{-3}$, exposed to strong ultraviolet radiation, $I(\mathrm{UV}) = 1 \times 10^5 I(\mathrm{Draine})$. In their model, carbon, oxygen, nitrogen and sulfur are taken to be undepleted, i.e. everything is in the gas phase, whereas silicon is depleted by a factor of only 10. Thus they find distinct zones in which S^+, Si^+ and S dominate the chemistry, which do not occur in our model. Since their model does not include metals other than silicon, carbon and sulfur dominate the ionization balance

Table 6. Column densities (in cm^{-2}) from two-dimensional model calculations

	Model				Observed
	Full 2-dim		Semi		
	T1	T3	1-dim	1-dim[b]	
A_V	6.7[a]	6.6[a]	6.6[a]	6.79	6.7
H_2	5.0 (21)	5.0 (21)	5.0 (21)	5.0 (21)	5.0 (21)
H	3.9 (20)	2.5 (20)	3.4 (20)	5.6 (20)	≈4.0 (20)
C	4.1 (16)	2.8 (16)	5.0 (16)	6.8 (16)	3.7 (16)
C^+	1.5 (17)	1.1 (17)	1.2 (17)	1.3 (17)	2.0 (17)
CO	2.9 (17)	2.8 (17)	3.1 (17)	3.2 (17)	3.0 (17)
^{13}CO	3.7 (15)	4.5 (15)	4.9 (15)	5.2 (15)	3.9 (15)
CS	6.5 (12)	9.2 (11)	6.5 (12)	1.1 (13)	9.5 (12)
CN	1.3 (13)	1.3 (13)	1.5 (13)	2.6 (13)	2.7 (13)
HCN	5.8 (12)	5.5 (12)	5.3 (12)	1.4 (13)	4.0 (13)
HCO^+	5.2 (12)	5.9 (12)	6.8 (12)	2.0 (12)	8.0 (12)
H_2CO	4.2 (12)	3.1 (12)	3.9 (12)	8.6 (12)	5.0 (12)
C_2H	1.5 (13)	9.9 (12)	1.8 (13)	4.6 (13)	1.8 (13)
N_2H^+	2.6 (11)	3.7 (11)	2.3 (11)	2.0 (11)	2.9 (11)

[a] This value was fixed to set the size of the cloud; The column densities refer to the shaded area in Fig. 9.
[b] Model 1 of Table 3.

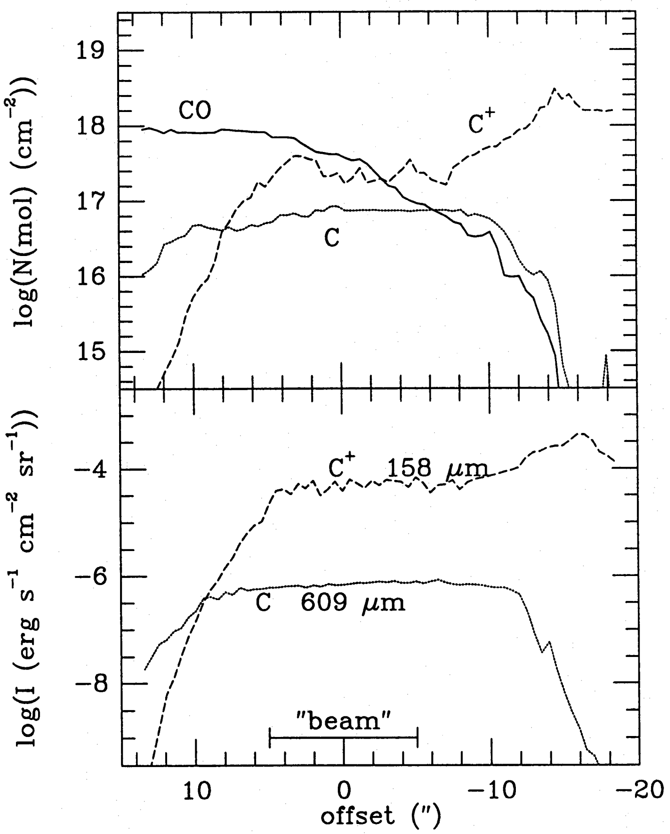

Fig. 10. Calculated column densities of C^+, C and CO (upper panel) and [C II] 158μm and [C I] 609μm intensities (lower panel) as functions of the position along the cross-cut through the two-dimensional model following the white arrow. The ($0''$, $0''$) position refers to the observed position

in the cloud, causing the chemistry to be quite different from our models. Molecular oxygen is removed in the dark cloud part of their model through the reactions

$$\begin{aligned} &O_2 + S \rightarrow SO + O \\ &O_2 + Si \rightarrow SiO + O \end{aligned} \qquad (29)$$

whereas in our models, only removal through C^+, He^+ and photodissociation plays a role, due to the lower gas-phase abundances of sulfur and silicon. A similar situation occurs with the reactions

$$\begin{aligned} &H_2O + Si^+ \rightarrow SiOH^+ + H \\ &SiOH^+ + e \rightarrow Si + OH \end{aligned} \qquad (30)$$

which form an important removal channel of water and a major source of OH in their paper. However, even with all of the sulfur in the gas phase, the models of Sternberg & Dalgarno (1994) can barely explain the observed high H_2S column density of $7 \times 10^{12}\,\mathrm{cm}^{-2}$, and this model would then overproduce CS and SO. Most of the other differences between their paper and ours stem from the higher efficiency of neutral-neutral reactions at the higher densities and temperatures in the model of Sternberg & Dalgarno (1994).

In order to compare our PDR model with that of Fuente et al. (1993, hereafter FMCB), we have performed model calculations for NGC 7023. This is a cloud with parameters close to those of IC 63; FMCB list $n_H = 1 \times 10^4\,\mathrm{cm}^{-3}$ (model 2 of table 10 of FMCB) or $1 \times 10^5\,\mathrm{cm}^{-3}$ (model 4), $\zeta_{CR} = 5 \times 10^{-17}\,\mathrm{s}^{-1}$, $A_V = 6$ mag and a radiation field of 2600 Habing units (≈ 3000× the Draine field). The temperature is kept fixed at 30 K, so heating and cooling are ignored in these models. Following FMCB we take the gas-phase fractions of C, N and O to be 10 %. Their model only includes Fe as a metal with a concentration

[Fe] = 1.5×10^{-8}, corresponding to a gas-phase fraction δFe = 0.00035. To include the other metals and sulfur into the calculations, we have followed two different approaches, leading to models N1 and N2 of Table 7. In model N1 we used a fixed value of δM = 0.00035 for all metals including S. In the second model, we followed the same path as in our IC 63 models, in giving all metals an abundance that is a fixed fraction of the ζ Oph gas-phase fractions; based on iron, this fraction is 0.13. Results of these models, along with observed values and model calculations from FMCB are listed in Table 7.

Table 7. Results of model calculations for NGC 7023

Model	FMBC	N1	N2	Observed
A_V (mag)	6.0	6.2	5.9	...
H_2	...	4.0 (21)	4.0 (21)	7.4 (21)
^{13}CO	...	2.7 (15)	2.4 (15)	6.0 (15)
$C^{18}O$	...	1.3 (14)	9.7 (13)	9.5 (14)
CS	...	2.2 (11)	1.4 (13)	1.3 (12)
CN	7.6 (12)	4.5 (13)	3.5 (13)	1.0 (13)
HCN	2.6 (13)	2.0 (12)	1.9 (12)	1.2 (12)
HNC	1.6 (11)	6.8 (11)	7.5 (11)	8.5 (11)
HCO^+	1.1 (14)	1.3 (13)	4.7 (12)	1.0 (12)
$H^{13}CO^+$	...	2.3 (11)	8.7 (10)	<2.3 (11)
C_2H	1.7 (15)	4.2 (13)	3.5 (13)	<3.1 (13)
N_2H^+	9.6 (11)	4.5 (11)	2.5 (11)	<3.9 (12)

Gas phase fractions: δC = 0.10, δO = 0.10, δN = 0.10, I_{UV} = $3000 I$(Draine); Metals including sulfur: model N1: δM = 0.00035; model N2: δM = 0.13 × δM(ζ Oph). The model refers to offset position ($-10''$, $20''$) of the observations.

Due to the low metal fraction in model N1, all free electrons are supplied by ionized carbon, even in the dark cloud region. As a result, recombination of ions like HCO^+ and N_2H^+ is slow, and these species are produced in large amounts, comparable to the models of FMCB, which are much larger than the observed column densities. Model N2 has a higher electron abundance, and this decreases the abundances of HCO^+ and N_2H^+. It also slows down the ion-driven chemistry, resulting in less HCN, HNC and C_2H. This model seems to reproduce the observations fairly well.

Other differences between our model and the model of FMCB arise from our explicit treatment of the CO self-shielding processes. This detailed treatment causes the $C^+ \rightarrow C \rightarrow CO$ transition, and thus all of the chemically different regions, to shift to lower A_V. For example in FMCB the radicals peak near $A_V \approx 4.5$ mag, whereas in our model this peak occurs at $A_V \approx 3$ mag. Note, however, that our models fail to reproduce the observed ^{13}CO and $C^{18}O$ column densities, unless the H_2 column density is increased. Unfortunately, FMCB do not list their model results for these species.

The published NGC 7023 models of FMCB do not include sulfur, and they therefore do not give a fit for the CS column density. The fact that our model N2 overproduces CS by a factor of about 10 might indicate that in NGC 7023, like in IC 63, sulfur is less abundant in the gas-phase than most heavy elements, compared to the values measured toward ζ Oph.

9. Conclusions

Chemical models have been developed for the photon dominated region IC 63 in order to reproduce the observed molecular column densities. The code uses the actual spectrum of the illuminating star γ Cas, and computes the photo-rates directly at each depth step using the cross sections for photodissociation or photoionization as functions of wavelength. Shielding by dust particles and by coincident lines of H and H_2 is included, as well as self-shielding. The temperature structure is computed by taking explicitly the heating and cooling processes into account.

The model demonstrates that the PDR consists of a number of distinct zones, each with a different chemistry and composition. From the edge inward these are the C^+ to C conversion zone, the "radical region", the "atomic oxygen region" and the dark cloud region. The simple, one-dimensional model succeeds quite well in explaining the observed column densities. Especially the good fit for the C^+ / C / CO abundances is significant, since it implies a low gas-phase carbon abundance of only (12 ± 4) % (paper III). The current models fail, however, to reproduce all aspects of the sulfur chemistry; if the gas-phase sulfur abundance is fixed to reproduce the observed CS column density, the models produce too little H_2S and too much SO by an order of magnitude. It may be that some important reactions have not yet been included in our network, particularly those involving grain chemistry. To what extent such reactions can affect the abundances of other species, like H_2O, NH_3, CH_4 and H_2CO needs to be investigated. The computed temperature structure of the cloud agrees quite well with observational diagnostics. The two-dimensional models essentially confirm these results, but they illustrate that the actual geometry of the cloud is of prime importance, especially for the temperature structure.

The fact that we can reproduce most observed column densities as well as other characteristics, such as the H_2 ultraviolet spectrum and the temperature structure, in a simple PDR like IC 63 is encouraging. It means that the physical and chemical processes in such an environment are now reasonably well understood, so that they can be applied with enhanced confidence to more complex PDRs.

Acknowledgements. We like to thank John Telting and Rens Waters for supplying us with the IUE data on γ Cas. We are also grateful to W. McCutcheon for making the HI map of IC 63 available prior to publication. We further wish to thank Tom Millar for useful discussions about the chemical network. Research in astrochemistry in Leiden is supported by the Netherlands Organization for Scientific Research (NWO) and at the University of Arizona by NASA through grants NAGW–2255 and –4126.

References

Allison, A.C., Dalgarno, A., 1970, Atomic Data 1, 289
Atkinson, R., Baulch, D.L., 1989, J. Phys. Chem. Ref. Data 18, 881

Anders, E., Grevesse, N., 1989, Geochim. Cosmochim. Acta 53, 197

Bakes, E.L.O., Tielens, A.G.G.M., 1994, ApJ 427, 822

Bennett, A., 1988, in: Rate coefficients in Astrochemistry, p339 eds. T.J. Millar, D.A. Williams, (Kluwer)

Black, J.H., van Dishoeck, E.F., 1987, ApJ 322, 412

Blake, G.A., Ancich, V.G., Huntress, W.T., 1986, ApJ 300, 415

Bontekoe, T.R., Koper, E., Kester, D.J.M., 1994, A&A 284, 1037

Cardelli, J.A., Mathis, J.S., Ebbets, D.C., Savage, B.D. , 1993, ApJ 402, L17

Chambaud, G., Launay, J.M., Levy, B., Millie, P., Roueff, E., Tran Minh, F., 1980, J. Phys. B 13, 4205

Craven, W., Murrell, J.N., 1987, J.Chem.Soc.Faraday Trans.II, 83, 1733

Code, A.D., Meade, M.R., 1979, ApJS 39, 195

de Jong, T., 1977, A&A 55, 137

d'Hendecourt, L.B., Leger, A., 1987, 180, L9

Draine, B.T., 1978, ApJS 36, 595

Drdla, K., Knapp, G.R., van Dishoeck, E.F., 1989, ApJ 345, 815

Dressler, K., Wolniewicz, L. 1985, J. Chem. Phys. 82, 4720

Federman, S.R., Danks, A.C., Lambert, D.L., 1984, ApJ 287, 219

Fuente, A., Martin-Pintado, J., Cernicharo, J., Bachiller, R., 1993, A&A, 276, 473 (FMCB)

Genzel, R., Harris, A.I., Stutzki, J., 1991, in: Proceedings of the 22nd Eslab Symposium on Infrared Spectroscopy in Astronomy, ed. A.C.H. Glasse (Paris: ESA)

Goldsmith, P.F., Irvine, W.M., Hjalmarson, Å, Elldér, J., 1986, ApJ 310, 383

Grevesse, N., Lambert, D.L., Sauval, A.J., Van Dishoeck, E.F., Farmer, C.B., Norton, R.H., 1991, A&A 242, 488

Herbst, E., Lee, H.-H., Howe, D.A., Millar, T.J., 1994, MNRAS 268, 335

Herd, C.R., Adams, N.G., Smith, D., 1990, ApJ 349, 388

Horiguchi, T., et al., 1994, PASJ 46, 9

Irvine, W.M., Schloeb, F.P., Hjalmarson, Å., Herbst, E., 1985, in: Protostars and planets II, eds. D.C. Black & M.S. Matthews (Tucson: University of Arizona Press)

Jansen, D.J., Van Dishoeck, E.F., Black, J.H., 1994, A&A 282, 605 (Paper I)

Jansen, D.J., van Dishoeck, E.F., Black, J.H., Keene, J., 1994, in: Proceedings of the 2nd Köln-Zermatt Symposium, in press

Jansen, D.J., van Dishoeck, E.F., Keene, J., Betz, A., Boreiko, R., 1995, A&A, to be submitted (Paper III)

Keene, J., Blake, G.A., Phillips, T.G., Huggins, P.J., Beichman, C.A., 1985, ApJ 299, 967

Köster, B., Störtzer, H., Stutzki, J., Sternberg, A., 1994, A&A 284, 545

Le Bourlot, J., Pineau des Forêts, G., Roueff, E., Flower, D.R. , 1993 A&A 267, 233

Lepp, S., Dalgarno, A., 1988, ApJ 335, 769

Macau-Hercot, D., Jamar, C., Monfils, A., Thompson, G.I., Houziaux, L., Wilson, R., 1978, Supplement to the Ultraviolet Bright Star Catalogue, (ESA SR-28, Paris)

Mathis, J.S., Mezger, P.G., Panagia, N., 1983, A&A 128, 212

Meyer, D.M., Jura, M., Hawkins, G.W., Cardelli, J.A., 1994, ApJ 437, L59

Millar, T.J., Rawlings, J.M.C., Bennett, A., Brown, P.D., Charnley, S.B., 1991, A&AS 87, 585

Mitchell, G.F., Deveau, T.J., 1983, ApJ 266, 646

Murakami, T., Koyama, K., Inoue, H., Agrawal, P.C., 1986, ApJ 310, L31

Parmar, A.N., Israel, G.L., Stella, L., White, N.E., 1993, A&A 275, 227

Piirola, V., 1979, A&AS, 38, 193

Pineau des Forêts, G., Roueff, E., Schilke, P., Flower, D.R., 1993, MNRAS 262, 915

Prasad, S.S., Huntress, W.T., 1980, ApJS 43, 1

Prasad, S.S., Huntress, W.T., 1982, ApJ 260,590

Roberge, W.G., Jones, D., Lepp, S., Dalgarno, A., 1991, ApJS 77, 287

Savage, B.D., Cardelli, J.A., Sofia, U.J., 1992, ApJ 401, 706

Schilke, P., Walmsley, C.M., Pineau des Forêts, G., Roueff, E., Flower, D.R., Guilloteau, S., 1992, A&A 256, 595

Shalabiea, O.M., Greenberg, J.M., 1994, A&A 290, 266

Smith, D., Spañel, P., 1993, Chem. Phys. Lett. 211, 454

Sosin, C., Van Dishoeck, E.F., Black, J.H., 1990, unpublished results

Spaans, M., 1995, A&A, submitted

Stephens, T.L. , Dalgarno, A., 1972, J. Quant. Spectrosc. Rad. Tranf. 12, 569

Sternberg, A. 1988, ApJ 332, 400

Sternberg, A. 1989, ApJ 347, 863

Sternberg, A., Dalgarno, A., 1989, ApJ 338, 197

Sternberg, A., Dalgarno, A., 1995, ApJS, in press

Stutzki, J., Stacey, G.J., Genzel, R., Harris, A.I., Jaffe, D.T., Lugten, J.B., 1988, ApJ 332, 279

Suzuki H., Yamamoto, S., Ohishi, M., Kaifu, N., Ishikawa, S., Hirahara, Y., Takano, S., 1992, ApJ 392, 551

Tauber, J.A., Tielens, A.G.G.M, Meixner, M., Goldsmith, P.F., 1994 ApJ 422, 136

Telting, J.H., Kaper, L., 1994, A&A 284, 515

Tielens, A.G.G.M., Hollenbach, D., 1985, ApJ 291, 722

Troy, B.E., Johnson, C.Y., Young, J.M., Holmes, J.C., 1975, ApJ, 195, 643

Van Dishoeck, E.F., 1987, in: Rate Coefficients in Astrochemistry eds. T.J. Millar & D.A. Williams (Dordrecht: Kluwer)

Van Dishoeck, E.F., 1994, in: The first symposium on the Infrared cirrus and diffuse interstellar clouds, eds. R.M. Cutri & W.B. Latter (San Fransisco: Astronomical Society of the Pacific)

Van Dishoeck, E.F., Black, J.H., 1982, ApJ 258, 533

Van Dishoeck, E.F., Black, J.H., 1986, ApJS, 62, 109

Van Dishoeck, E.F., Black, J.H., 1988, ApJ, 334, 771

Van Dishoeck, E.F., Black, J.H., 1989, ApJ, 340, 273

Van Dishoeck, E.F., Jansen, D.J., Schilke, P., Phillips, T.G., 1993, ApJ 416, L83

Verstraete, L., Léger, A., d'Hendecourt, L., Dutuit, O., Défourneau, D., 1990, A&A 237, 436

Waters, L.B.F.M., Telting, J.H., 1993, priv.comm.

White, N.E., Swank, J.H., Holt, S.S., Parmar, A.N., 1982, ApJ 263, 277

Witt, A.N., Stecher, T.P., Boroson, T.A., Bohlin, R.C., 1989, ApJ 336, L21

Wolniewicz, L., Dressler, K. 1988, J. Chem. Phys. 88, 3861

This article was processed by the author using Springer-Verlag TEX A&A macro package 1992.